



Article

Integration of Satellite-Based Optical and Synthetic Aperture Radar Imagery to Estimate Winter Cover Crop Performance in Cereal Grasses

Jyoti S. Jennewein ^{1,*}, Brian T. Lamb ², W. Dean Hively ², Alison Thieme ³, Resham Thapa ^{1,4},
Avi Goldsmith ¹ and Steven B. Mirsky ¹

¹ USDA—Agricultural Research Service, Sustainable Agricultural Systems Laboratory, 10300 Baltimore Avenue, Beltsville, MD 20705, USA; rthapa@ncsu.edu (R.T.); avi.goldsmith@usda.gov (A.G.); steven.mirsky@usda.gov (S.B.M.)

² U.S. Geological Survey, Lower Mississippi-Gulf Water Science Center, Beltsville, MD 20705, USA; blamb@usgs.gov (B.T.L.); whively@usgs.gov (W.D.H.)

³ Department of Geographical Sciences, University of Maryland, College Park, MD 20742, USA; thieme@terpmail.umd.edu

⁴ Department of Crop and Soil Sciences, North Carolina State University, Raleigh, NC 27695, USA

* Correspondence: jyoti.jennewein2@usda.gov

Abstract: The magnitude of ecosystem services provided by winter cover crops is linked to their performance (i.e., biomass and associated nitrogen content, forage quality, and fractional ground cover), although few studies quantify these characteristics across the landscape. Remote sensing can produce landscape-level assessments of cover crop performance. However, commonly employed optical vegetation indices (VI) saturate, limiting their ability to measure high-biomass cover crops. Contemporary VIs that employ red-edge bands have been shown to be more robust to saturation issues. Additionally, synthetic aperture radar (SAR) data have been effective at estimating crop biophysical characteristics, although this has not been demonstrated on winter cover crops. We assessed the integration of optical (Sentinel-2) and SAR (Sentinel-1) imagery to estimate winter cover crops biomass across 27 fields over three winter–spring seasons (2018–2021) in Maryland. We used log-linear models to predict cover crop biomass as a function of 27 VIs and eight SAR metrics. Our results suggest that the integration of the normalized difference red-edge vegetation index (NDVI_RE1; employing Sentinel-2 bands 5 and 8A), combined with SAR interferometric (InSAR) coherence, best estimated the biomass of cereal grass cover crops. However, these results were season- and species-specific ($R^2 = 0.74, 0.81, \text{ and } 0.34$; $\text{RMSE} = 1227, 793, \text{ and } 776 \text{ kg ha}^{-1}$, for wheat (*Triticum aestivum* L.), triticale (*Triticale hexaploide* L.), and cereal rye (*Secale cereale*), respectively, in spring (March–May)). Compared to the optical-only model, InSAR coherence improved biomass estimations by 4% in wheat, 5% in triticale, and by 11% in cereal rye. Both optical-only and optical-SAR biomass prediction models exhibited saturation occurring at $\sim 1900 \text{ kg ha}^{-1}$; thus, more work is needed to enable accurate biomass estimations past the point of saturation. To address this continued concern, future work could consider the use of weather and climate variables, machine learning models, the integration of proximal sensing and satellite observations, and/or the integration of process-based crop–soil simulation models and remote sensing observations.

Keywords: winter cover crops; biomass; optical synthetic aperture radar integration; remote sensing; winter cover crop performance



Citation: Jennewein, J.S.; Lamb, B.T.; Hively, W.D.; Thieme, A.; Thapa, R.; Goldsmith, A.; Mirsky, S.B.

Integration of Satellite-Based Optical and Synthetic Aperture Radar Imagery to Estimate Winter Cover Crop Performance in Cereal Grasses. *Remote Sens.* **2022**, *14*, 2077.

<https://doi.org/10.3390/rs14092077>

Academic Editor: Zhenhong Li

Received: 28 February 2022

Accepted: 20 April 2022

Published: 26 April 2022

Publisher's Note: MDPI stays neutral with regard to jurisdictional claims in published maps and institutional affiliations.



Copyright: © 2022 by the authors. Licensee MDPI, Basel, Switzerland. This article is an open access article distributed under the terms and conditions of the Creative Commons Attribution (CC BY) license (<https://creativecommons.org/licenses/by/4.0/>).

1. Introduction

Planting cover crops is recognized as an important conservation practice to promote agricultural sustainability via the provisioning of agro-ecosystem services [1]. Some of these well-documented agro-ecosystem services include the protection of soil from erosion,

increased nutrient retention, reduction in nutrient leaching losses, reduction in disease and pest infestations, increased weed suppression, increased infiltration, reduced overland water flow, soil health improvements via carbon sequestration, and developing resilient cropping systems that better adapt and mitigate climate change [2–6]. Cover crop performance estimations, such as percent ground cover and biomass accumulation, are directly related to the magnitude of agro-ecosystem services that cover crops can provide [4,7,8]. Despite the well-recognized relationship between cover crop performance and the associated benefits to cropping systems, few studies to date have assessed the ability of remote sensing to estimate cover crop performance, especially at the landscape scale.

Remote sensing is a powerful tool capable of producing landscape-level assessments of cover crop presence and absence [9,10], emergence and termination [11,12], and performance [13–15]. To date, remote sensing in cover crop research has primarily employed optical sensing approaches using proximal (hand-held) sensors [14], unoccupied aerial vehicles (UAVs) [16,17], high-resolution aerial images [18], and Earth-observing satellites [8,10,13,19]. Optical vegetation indices (VIs) used to estimate plant biomass usually exploit the relationship between visible light with low reflectance (linked to plant pigment concentration) and high reflectance observed in near-infrared (NIR) light (influenced by internal leaf structure) [20]. This visible-NIR reflectance difference is enhanced during plant growth and manifests as increased fractional cover, which is linked to plant biomass. Both the triangular vegetation index (TVI) [21] and the normalized difference vegetation index (NDVI) [22] exploit the visible-NIR difference and have been used to successfully estimate biomass in cereal grass cover crop species [13,14].

VIs derived from optical imagery, particularly NDVI, tend to saturate at a leaf area index (LAI) greater than three in numerous plant species [23,24]. Similarly, previous work observed NDVI saturation at approximately 1500 kg ha⁻¹ biomass in cereal grass species [14]. This substantially limits our ability to estimate biomass values at the higher ranges (i.e., >1500 kg ha⁻¹) that are frequently observed in the springtime, particularly in late-terminated cover crop fields under warmer growing conditions. Although red-edge bands were shown to be more resistant to saturation [17,24–26] they have only recently been incorporated into earth-observing platforms such as the European Space Agency's (ESA) Sentinel-2 satellites (launched in June 2015 and March 2017). Sentinel-2 satellites contain three red-edge bands and have a 20-m spatial resolution and a five-day revisit time, resulting in a greater spatial and temporal resolution than Landsat satellites. Red-edge indices such as the normalized difference red-edge index (NDVI_RE) and the simple ratio red-edge (SR_RE) have shown strong relationships with chlorophyll A [27], which, in turn, is closely linked with crop biophysical characteristics such as LAI and fractional ground cover [28,29]. Additionally, previous work demonstrated that the visibly atmospherically resistant index using a red-edge band (VARI_RE) was better able to predict the LAI of corn (*Zea mays* L.) past the point of saturation (i.e., up to LAI values of six) [30]. In contrast, other studies found that red-edge-based indices did not improve biomass estimation in corn and soybeans (*Glycine max* L.) when compared to traditional VIs such as NDVI [31]. In addition to red-edge based indices, new VIs, such as the NIR reflectance of vegetation index (NIRv) [32] and kernel NDVI (kNDVI) [33], have also been developed to address saturation issues with optical remote sensing. NIRv has shown good agreement with gross primary production (GPP) in corn and soybeans [32]. Finally, kNDVI is a nonlinear generalization of NDVI that is more resistant to saturation [33] and, therefore, may also be useful in estimating higher cover crop biomass levels beyond the point of saturation.

Active remote sensing approaches such as synthetic aperture radar (SAR) also have emerged as a viable technique for monitoring and estimating crop biophysical characteristics [34–36], although most studies focus on the use of SAR data in crop classification. SARs operate at microwave wavelengths (0.18–30 cm), emit coherent signals, and measure the backscattered intensity (backscatter) and phase of the return signals. The intensity and phase of the return signal at a given frequency and polarization can be used to elucidate the 'polarimetric signatures' of landscape features based on the type of scattering that is

present [37]. Agricultural studies have most commonly utilized SAR imagery in either the L-band (15–30 cm) or C-band (3.75–7.5 cm) wavelength ranges, often with two linear polarizations (dual-pol) or four linear polarizations (quad-pol). The unique information contained in SAR polarimetric channels, such as a change from transmitted horizontal (H) to return vertical (V) backscatter or from V to H (i.e., cross-polarization), provides information on the presence of volume scattering targets. Vegetation exhibits strong volume scattering; thus, cross-polarization backscatter has been shown to be well correlated with total biomass in wheat (*Triticum aestivum* L.) and soybeans [38,39]. Similarly, the radar vegetation index (RVI), which is produced using co- and cross-polarization backscatter, has been shown to be sensitive to vegetation water content and LAI [40].

In addition to the backscatter intensity, SAR signals also contain phase information. Combining polarimetric backscatter and polarimetric phase information provides additional information, allowing for more refined classifications of ground targets with the use of polarimetric decompositions [36]. For instance, the polarimetric parameters decomposed from SAR data—such as entropy, anisotropy, and alpha angle—can successfully predict crop biophysical characteristics such as biomass and height under certain conditions [41–43]. Finally, the cross-channel correlation coefficient known as the interferometric SAR (InSAR) coherence compares the phase information from two repeat-pass SAR images. When phase differences are similar for a neighborhood of pixels, InSAR coherence values will be high, and when phase differences are random, InSAR coherence values will be low. Reductions in InSAR coherence are often indicative of changes in target properties between two images, such as changes in soil roughness, soil moisture, vegetation water content, and vegetation structure [44,45]. However, InSAR coherence may also be useful in biomass estimation, as it quantifies phase change between two images and can, therefore, be used to estimate crop height [46,47] and growth [48]. Although the use of SAR to estimate crop biophysical characteristics is on the rise, few studies to date have integrated both optical and SAR data [49]. Moreover, to our knowledge, none focus specifically on small-stature winter cover crops that undergo a unique phenological development that includes fall establishment followed by a winter dormancy period and later springtime growth.

The ESA's publicly available multispectral (Sentinel-2) and SAR (Sentinel-1; dual polarization, C-band) satellite imagery provides a unique opportunity to assess the efficacy of linking contemporary VIs using red-edge bands and SAR-derived metrics such as backscatter intensities, polarimetric parameters, and InSAR coherence. When integrated, these two data streams may enable a more accurate prediction of winter cover crop biomass beyond the previously identified saturation points. Thus, our first objective was to determine which optical index from Sentinel-2 was best-suited to estimating the cover crop biomass. Secondly, we evaluated whether the addition of SAR backscatter intensities, polarimetric parameters, and InSAR coherence to optical data increased our ability to estimate cover crop biomass, especially over 1500 kg ha^{-1} [14]. We hypothesized that: (1) non-normalized, red-edge indices would outperform other VIs for estimating winter cover crop biomass and (2) that the integration of optical and SAR metrics would result in better biomass estimation in winter cover crops. To test these hypotheses, we collected destructive biomass samples over three winter–spring cover crop growing seasons from cover crop fields planted with cereal grass species at the U.S. Department of Agriculture (USDA), Beltsville Agricultural Research Center (BARC) facility located in Beltsville, Maryland, United States, and regressed a suite of remote sensing measures to biomass.

2. Methods

2.1. Study Area and Sampling Plan

We sampled 27 cover crop fields (~5 sampling locations per field) over three winter-to-spring seasons (2018–2019, 2019–2020, and 2020–2021) at the USDA-BARC research facility (Figure 1). These fields were planted with one of the three cereal grass cover crop species: wheat ($n = 431$ across 10 fields), 'Aroostook' cereal rye (*Secale cereale*; $n = 153$ across 14 fields), and triticale (*Triticale hexaploide* Lart.; $n = 185$ across six fields). Cover crops were

planted between 26 September and 18 October of a given year, after harvest of the previous summer crop (usually corn, soybeans, or alfalfa (*Medicago sativa*)). Some of the fields—those in triticale and some wheat—were fertilized in the fall, as these fields were harvested later in the spring of the following year (typically in April) for dairy silage production.

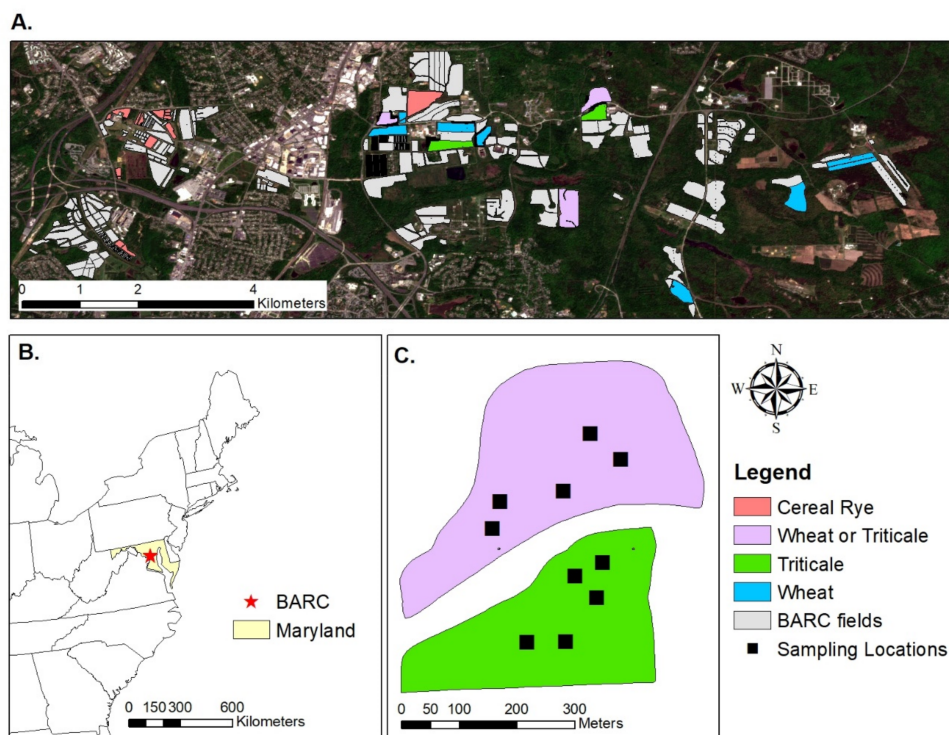


Figure 1. Overview of the study area located at the Beltsville Agricultural Research Center (BARC) in Maryland (A,B). Study fields (2019–2021) are colored by species. Some fields (purple) were used by wheat and triticale in different years of the study. Approximately five flagged locations were sampled within each field at a given sampling time or event (C). (A) contains a Sentinel-2 satellite image from 1 May 2020; (B) uses a map of the United States, courtesy of the Federal Government.

During the 2019–2020 and 2020–2021 seasons, we sampled approximately five locations per field at each sampling time. The sampling dates were distributed throughout the cover crop growth period: once per month from October–February, twice per month from March–April, and once in May. We performed more frequent sampling in the springtime due to the faster cover crop growth and development. Sampling locations were kept consistent within seasons. During the spring of 2019, we collected cover crop biomass twice (late April–early May). We flagged five sampling locations per field with the goal of capturing spatial variability in cover crop performance (i.e., capturing areas of low and high biomass). Across all seasons, we selected sampling locations with locally uniform growth towards the center of each field to avoid edge effects and mixed pixels. Samples were spaced at least 30 m apart to avoid collections within the same pixel.

Destructive biomass samples were collected near flagged locations within each field. At each flag, we sampled aboveground cover crop biomass from $\sim 0.57 \text{ m}^{-2}$ areas in paper bags (i.e., harvested 1-m length cover crop from three adjacent drilled rows that were 19 cm apart). Paper bags containing fresh biomass samples were then dried in an oven for approximately one week at $60 \text{ }^{\circ}\text{C}$ and the dry weights were recorded. We then scaled these values from g m^{-2} to kg ha^{-1} .

During the 2019–2020 and 2020–2021 growing seasons, we also collected a series of nadir photographs from a red, green, blue (RGB) Canon PowerShot G16 camera (12.1 megapixels). In previous work, nadir photographs were used to estimate fractional vegetative cover [14]. However, as we did not have complete time series photographs associated with every

sampling event, we could not include fractional vegetative cover as a covariate in our analysis. Instead, we used photographs and estimates of fractional vegetative cover where possible to interpret the relationship between the remotely sensed data and the destructively sampled biomass. We calculated fractional vegetative cover for each photograph by applying threshold values to the digital numbers for red/green ratio [50] and excess green [51] VIs.

2.2. Growing Degree Days

We calculated growing degree days (GDD) to assess inter-annual weather differences in cover crop growth across our study years. We used a combination of weather station data from 2019 to 2020 at BARC and the daily Daymet [52,53] estimations from a local weather station in Beltsville in 2021 to calculate GDD using the following equation:

$$\text{GDD} = \left[\frac{T_{\max} + T_{\min}}{2} \right] - T_{\text{base}}$$

where T_{\min} and T_{\max} were the daily minimum and maximum temperatures. We used 4 °C for T_{base} , based on prior studies for small-grain crops [14,54].

2.3. Soil Moisture Collections and Analyses

Sentinel-1 transmits C-band signals, which do not penetrate deeply into the soil column, and instead interact primarily with the soil surface. Because C-band signals respond strongly to moisture content, we calculated the correlation coefficients of four Sentinel-1 backscatter indices (VV, VH, VV/VH, and RVI) relative to measured values of soil volumetric water content (VWC) collected using a handheld sensor. Handheld collections were taken with an Acclima SDI-12 sensor in conjunction with Sentinel-1 overpasses at each of the fields on five dates in 2021 (March: 2nd, 15th, 26th, and April: 19th and 29th). Seven surface level measurements at 2 cm depth were taken near each plot, with six being taken within a 0.5 m radius of the center of the plot and the seventh in the center.

2.4. Sentinel-2 Imagery Acquisition and Processing

We procured level 2A Sentinel-2 reflectance products from ESA's Copernicus service and extracted the band reflectance for nine bands at the 20-m pixel resolution, including blue (B2), green (B3), red (B4), three red edge bands (B5, B6, B7), narrow band NIR (B8A), and two shortwave infrared bands (SWIR, B11 and B12). We selected the image acquisition that corresponded most closely to each destructive biomass sampling date. We applied the provided 20-m resolution cloud mask at the strictest level (i.e., 0) to remove clouds and cloud shadows. In total, we used 21 scenes and out of 769 plot-date measurements 180 samples were removed from the analysis due to the presence of clouds or cloud shadows. We also removed 16 observations that had a gap of >6 days between destructive sampling and the satellite image acquisition (mean image gap = ~3 days, standard deviation of image gap = ~2 days). This resulted in a total of 573 observations [55] for three cereal grass species (cereal rye: $n = 94$, triticale: $n = 158$, and wheat: $n = 321$). Next, we extracted band reflectance data to calculate 27 VIs (Table 1). These VIs were selected with a focus on (1) red-edge indices ($n = 14$) and (2) previously identified indices sensitive to biomass or similar plant characteristics, such as LAI, height, or leaf/stem density ($n = 13$). We processed the acquired images and extracted band reflectance using the 'raster' [56] and 'sf' [57] packages in the R statistical environment [58].

Table 1. List of optical vegetation indices (VIs) calculated from Sentinel-2 imagery where ρ indicates reflectance of a given optical band, RE_x indicates a red-edge optical band (which can be either band 5, 6 or 7 depending on the index variant), and SWIR_x indicates a shortwave infrared band (with band 11 or 12 depending on index variant).

Abbreviation	Parameter	Formula	Citation
NDVI_RE1	Red-edge normalized difference vegetation index (B5)	$\frac{(\rho_{\text{NIR}} - \rho_{\text{RE}_x})}{(\rho_{\text{NIR}} + \rho_{\text{RE}_x})}$	[31,59]
NDVI_RE2	Red-edge normalized difference vegetation index (B6)		
NDVI_RE3	Red-edge normalized difference vegetation index (B7)		
NDRE	Normalized difference red-edge index	$\frac{(\rho_{\text{RE}(B6)} - \rho_{\text{RE}(B5)})}{(\rho_{\text{RE}(B6)} + \rho_{\text{RE}(B5)})}$	[60,61]
SR_RE1	Simple ratio red-edge index (B5)	$\frac{\rho_{\text{NIR}}}{\rho_{\text{RE}_x}}$	[31]
SR_RE2	Simple ratio red-edge index (B6)		
SR_RE3	Simple ratio red-edge index (B7)		
RER	Red-edge ratio index	$\frac{\rho_{\text{RE}(B7)}}{\rho_{\text{RE}(B6)}}$	[29,62]
RTVI1	Red-edge triangular vegetation index (B5)	$100 * (\rho_{\text{NIR}} - \rho_{\text{RE}_x}) - 10 * (\rho_{\text{NIR}} - \rho_{\text{Green}})$	[31,63]
RTVI2	Red-edge triangular vegetation index (B6)		
RTVI3	Red-edge triangular vegetation index (B7)		
VARI_RE1	Visibly atmospherically resistant index red-edge (B5)	$\frac{(\rho_{\text{RE}_x} - 1.7 * \rho_{\text{Red}} - 0.7 * \rho_{\text{Blue}})}{(\rho_{\text{RE}_x} + 2.3 * \rho_{\text{Red}} - 1.3 * \rho_{\text{Blue}})}$	[30]
VARI_RE2	Visibly atmospherically resistant index red-edge (B6)		
VARI_RE3	Visibly atmospherically resistant index red-edge (B7)		
VARI_green	Visibly atmospherically resistant index green	$\frac{(\rho_{\text{Green}} - \rho_{\text{Red}})}{(\rho_{\text{Green}} + \rho_{\text{Red}} - \rho_{\text{Blue}})}$	[30]
TVI	Triangular Vegetation index	$0.5 * [120 * (\rho_{\text{NIR}} - \rho_{\text{Green}}) - 200 * (\rho_{\text{Red}} - \rho_{\text{Green}})]$	[14,21,64]
MTVI2	Modified triangular vegetation index 2	$\frac{1.5 * [1.2 * (\rho_{\text{NIR}} - \rho_{\text{Green}}) - 2.5 * (\rho_{\text{Red}} - \rho_{\text{Green}})]}{\sqrt{(2 * \rho_{\text{NIR}} + 1)^2 - (6 * \rho_{\text{NIR}} - 5 * \rho_{\text{Red}}) - 0.5}}}$	[65]
MCARI2	Modified Chlorophyll Absorption Ratio Index 2	$\frac{1.5 * [2.5 * (\rho_{\text{NIR}} - \rho_{\text{Red}}) - 1.3 * (\rho_{\text{NIR}} - \rho_{\text{Green}})]}{\sqrt{(2 * \rho_{\text{NIR}} + 1)^2 - (6 * \rho_{\text{NIR}} - 5 * \rho_{\text{Red}}) - 0.5}}}$	[65]
NDVI	Normalized difference vegetation index	$\frac{(\rho_{\text{NIR}} - \rho_{\text{Red}})}{(\rho_{\text{NIR}} + \rho_{\text{Red}})}$	[13,14,22]
kNDVI	Kernel normalized difference vegetation index	$\text{Tanh}(\text{NDVI}^2)$	[33]
NIRv [66]	Near-infrared reflectance of vegetation index	$\rho_{\text{NIR}} * \text{NDVI}$	[32]
SR	Simple ratio vegetation index	$\frac{\rho_{\text{NIR}}}{\rho_{\text{Red}}}$	[67]
SAVI	Soil adjusted vegetation index	$(1 + 0.5) * (\rho_{\text{NIR}} - \rho_{\text{Red}}) / (\rho_{\text{NIR}} + \rho_{\text{Red}} + 0.5)$	[64,68]
EVI	Enhanced vegetation index	$2.5 * (\rho_{\text{NIR}} - \rho_{\text{Red}}) / (1 + \rho_{\text{NIR}} + 6 * \rho_{\text{Red}} - 7.5 * \rho_{\text{Blue}})$	[64,68]
NDWI1	Normalized difference water index (B11)	$\frac{(\rho_{\text{NIR}} - \rho_{\text{SWIR}_x})}{(\rho_{\text{NIR}} + \rho_{\text{SWIR}_x})}$	[69]
NDWI2	Normalized difference water index (B12)		
SR_WI	Simple ratio water index	$\frac{\rho_{\text{SWIR}_B11}}{\rho_{\text{SWIR}_B12}}$	

2.5. Sentinel-1 Data Acquisition and Processing

We used Google Earth Engine (GEE) [70] to process Sentinel-1 backscatter imagery with VH and VV polarizations. The Sentinel-1 ground range detected (GRD) scenes on GEE had previously been processed with ESA's Sentinel Application Platform (SNAP) toolbox (SNAP, 2021) using the processing sequence of: updating image orbit file, GRD image border noise removal, thermal noise removal, radiometric calibration, and geometric terrain correction (orthorectification). In addition to using the VH and VV backscatter imagery, we also calculated RVI by modifying the original quad-pol equation [40] to be suited for dual-pol as per [66]. We also further adapted the equation because the dual-pol modifications described in [66] included polarizations that are not present in Sentinel-1 (Table 2).

To perform polarimetric decompositions on the same Sentinel-1 scenes that are processed to backscatter in GEE, we downloaded these scenes in single-look-complex (SLC) format from ESA to the calculate polarimetric parameters of entropy, anisotropy, and alpha. Polarimetric decompositions were performed in SNAP toolbox using the following sequence: image calibration, C2 matrix computation, polarimetric speckle filtering (5×5

Refined Lee), H-Alpha dual-pol decomposition (window size = 5), and geometric terrain correction. To generate Sentinel-1 InSAR coherence imagery, we used the Alaska Satellite Facility (ASF) Hybrid Pluggable Processing Pipeline (HyP3) tool [71], which contains modified Copernicus Sentinel data 2021, processed by ESA). Sentinel-1 InSAR pairs were selected using the ASF SAR baseline tool to maintain the shortest possible temporal and perpendicular baselines (i.e., the greatest degree of temporal and spatial similarity between image acquisitions). We developed a selection protocol for the InSAR pairs ordered through HyP3, where the image with the later acquisition time in the InSAR pair was matched most closely to ground biomass sampling. Once image pairs were selected, we used the HyP3 tool to generate interferograms with embedded Gamma software, performing an interferogram generation with a 10×2 window size (smallest possible window size). The Sentinel-1 interferogram and associated InSAR coherence images output from this process resulted in a pixel size of approximately 40 m, meaning that the destructive biomass sampling of small plots (0.57 m^{-2}) was unlikely to significantly impact coherence estimation. As the backscatter imagery produced using GEE, polarimetric decomposition imagery, and InSAR coherence imagery were derived from the same Sentinel-1 images, their incidence angles were identical for a single image, and nearly identical for an InSAR pair. It is also important to note that the incidence angle of observation for the Sentinel-1 image time series was consistent over our study sites, exhibiting a spatiotemporal mean incidence angle of 41.31 degrees, with temporal standard deviation of 0.08 degrees, and a spatial standard deviation of 0.15 degrees.

Table 2. Sentinel-1 synthetic aperture radar (SAR) backscatter, polarimetric, and phase parameters where σ° indicates backscatter intensity per unit area, P_i represent the probabilities from the eigenvalues in the polarimetric decomposition, λ is the non-negative real eigenvalues of the diagonal matrix, alpha is the alpha angle, entropy (H) and anisotropy (A) are additional output parameters from the polarimetric decomposition, and InSAR coherence from an analysis in which the first and second scene are denoted as S_1 and S_2 , respectively.

Sentinel-1 Synthetic Aperture Radar Metrics		
VV	Vertical Transmit—Vertical Return Backscatter Intensity	$\sigma^\circ \text{ VV}$
VH	Vertical transmit—horizontal return backscatter intensity	$\sigma^\circ \text{ VH}$
VHVV	Ratio of VH to VV	$\frac{\sigma^\circ \text{ VH}}{\sigma^\circ \text{ VV}}$
RVI	Radar vegetation index	$\frac{(4\sigma^\circ \text{ VH})}{(\sigma^\circ \text{ VH} + \sigma^\circ \text{ VV})}$ [40,66]
H	Entropy	$-\sum_{i=1}^{i=3} P_i \log(P_i)$
A	Anisotropy	$\frac{\lambda_2 + \lambda_3}{\lambda_2 - \lambda_3}$ [72,73]
α	Alpha	$\sum_{i=3} P_i \alpha_i$
InSar coherence	Interferometric synthetic aperture radar coherence	$\frac{\{S_1 + S_2\}}{\sqrt{\{S_1\}^2 + \{S_2\}^2}}$ [44]

2.6. Statistical Analyses

All analyses were performed in the R statistical environment [58]. As the relationship between cover crop biomass and VIs is often non-linear [14], we fit three regression models to estimate cover crop biomass from optical data: (1) log-transformed, (2) polynomial, and (3) segmented regression. Regression models were evaluated using various measures: goodness-of-fit statistic (adjusted R^2), error measures such as the root mean square error (RMSE) and the mean absolute error (MAE), and model fit using Akaike’s Information Criterion for small sample sizes (AICc) [74]. We opted to use AICc over the traditional AIC to avoid overfitting our data, as the number of observations increases AICc and AIC

converge, whereas, for smaller sample sizes, AICc are penalized more heavily. AICc were calculated using the following equation:

$$\text{AICc} = 2k - 2\ln(\hat{L}) + \frac{2k^2 + 2k}{n - k - 1} \quad (1)$$

where k denotes the number of predictors in a model, \hat{L} represents the maximum likelihood, and n is the sample size.

Finally, we calculated AIC weights (AICw) for the log-linear and polynomial models. AICw quantifies the probability that a given model was the best model in the set of compared models—in our case, the best model among the 27 VIs compared for a given model type (e.g., log-linear). Note that AICc and AICw cannot be used to compare different model sets (i.e., log-linear vs. polynomial). We also checked for the normality and homoscedasticity of the residuals for each model. After identifying the best-performing optical index using the above steps (objective 1), we assessed whether there were seasonal- or species-level differences using analysis of variance (ANOVA) and slope and intercept contrasts in the R ‘emmeans’ package [75].

To assess whether the integration of optical and SAR data could improve our estimations of cover crop biomass (objective 2), we paired the best-performing optical index with each SAR metric ($n = 8$) individually. As with objective 1, these models were then evaluated using adjusted R^2 , RMSE, MAE, AICc, and AICw. If more than one SAR metric improved model fit (i.e., $\Delta\text{AICc} < -2$) and these metrics were not collinear (i.e., $r < 0.7$), we evaluated combined models with the optical index identified in objective 1 and multiple SAR variables. We used ANOVAs to assess whether models containing both optical and SAR data were significantly better than models with only optical predictors. Finally, we conducted cross-validation using a 70–30% train–test split iterated 100 times, and used adjusted R^2 , RMSE, and MAE to summarize these results.

3. Results

Cumulative GDD did not vary substantially among study years (Figure 2). Despite similarities in cumulative GDD during the cover crop growth period over the years, cover crop biomass production varied substantially. Destructively sampled cover crop biomass ranged from 141 to 4498 kg ha⁻¹ in spring 2019, from 3.5 to 8770 kg ha⁻¹ during 2019–2020, and from 30 to 5675 kg ha⁻¹ during 2020–2021.

We did find evidence of species-level differences in fractional vegetative cover at both low, medium, and high biomass levels (Figure 3). However, we did not have sufficient observations to conduct a formal analysis to determine whether these differences were statistically significant. At low biomass levels (~1000 kg ha⁻¹), triticale appears to have a higher fractional vegetative cover than cereal rye and wheat. As no cereal rye biomass levels exceeded 4000 kg ha⁻¹, we were not able to compare the highest biomass ranges between all three species. However, our in situ photographic data indicated that cereal rye was patchier than wheat and triticale at all biomass levels, with the caveat that we obtained limited cereal rye photographs and a gap of >7 days from photographs and biomass harvests in 2019–2020.

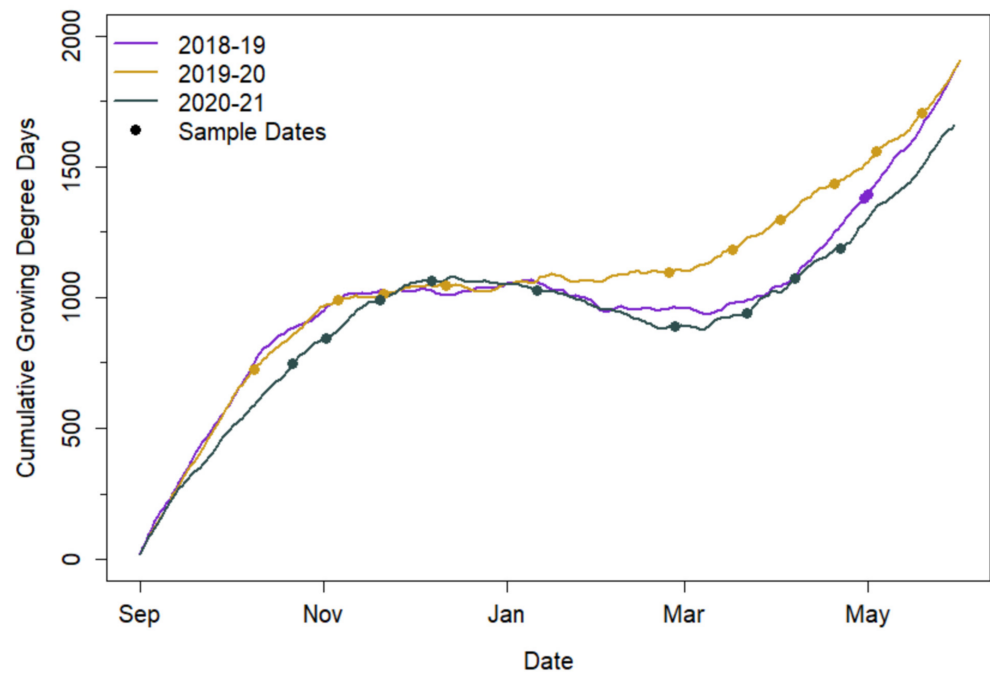


Figure 2. Accumulated growing degree days (GDD, including negative values) for study years (2018–2021) with sample dates (points).

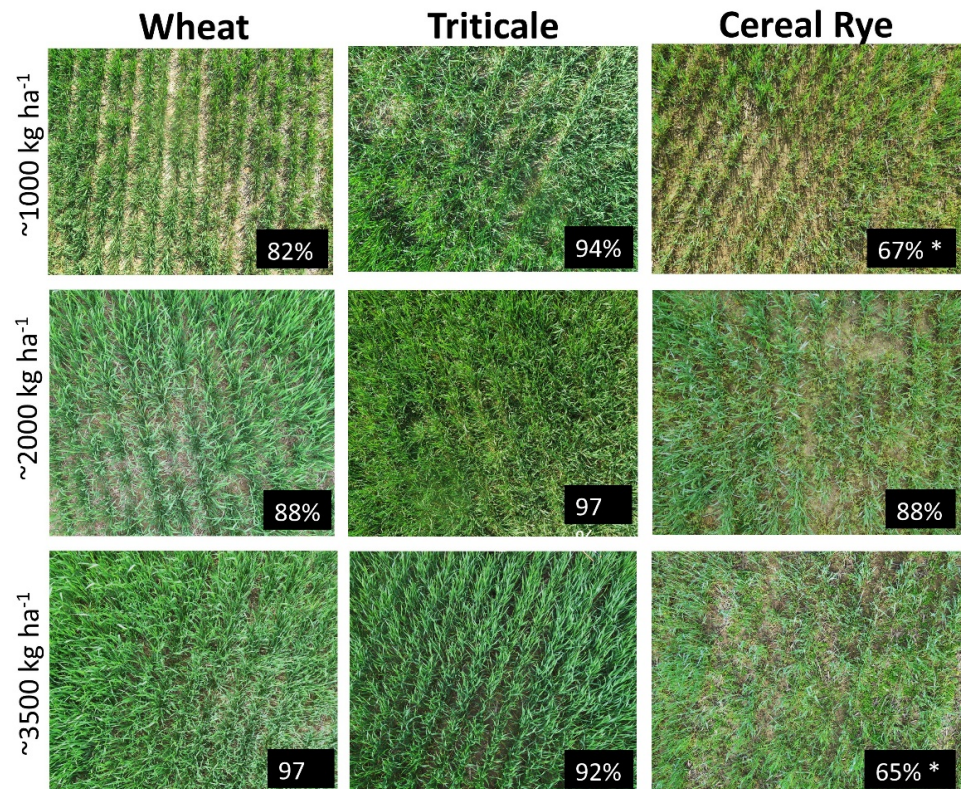


Figure 3. Monopole mounted (~3 m), nadir photographs of crop species at various biomass levels. Fractional vegetative cover estimates are displayed in the bottom right corner, and values with '*' indicates a difference in >7 days from when a photograph was collected and when that sample was harvested, dried, and weighed for biomass. Fractional vegetative cover was estimated empirically by applying threshold values for red–green ration and excess green optical vegetation indices.

We also examined the spectral response from Sentinel-2 for each species at a low and high biomass (Figure 4). As anticipated, we observed a greater NIR reflectance and decreased red reflectance at high biomass ($>3000 \text{ kg ha}^{-1}$) compared to low biomass ($<1000 \text{ kg ha}^{-1}$), which is, in part, related to the exposed soil present at low ground cover. Similarly, the reflectance of the first red-edge band (B5) decreased, while the second and third red-edge bands (B6 and B7) increased reflectance with increasing cover crop biomass levels. Interestingly, in the SWIR portion of the spectrum, reflectance from low biomass exceeded those of high biomass for all species, but the magnitude of this difference was smallest in cereal rye.

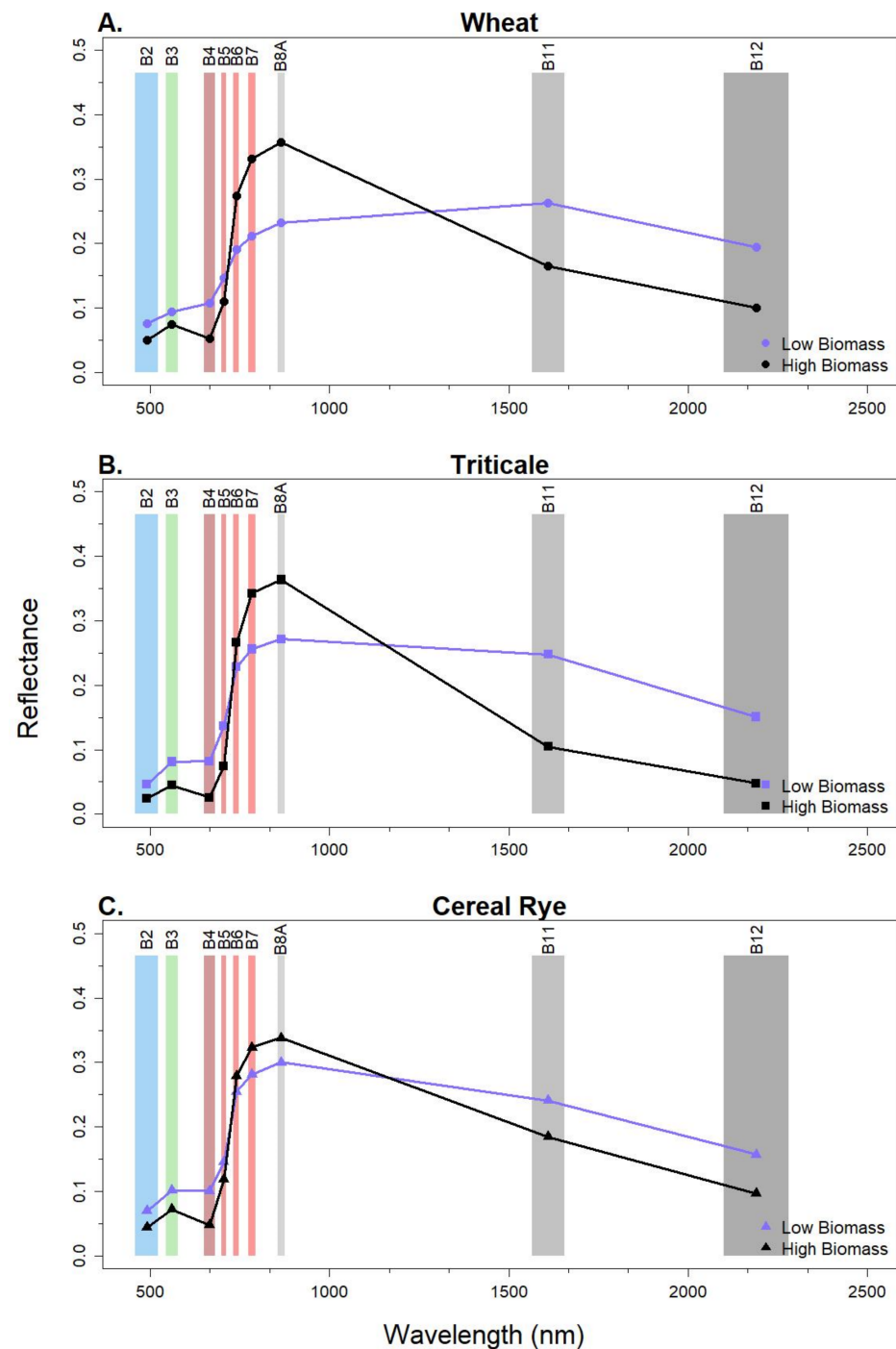


Figure 4. Example of spectral reflectance of high ($\sim 3500 \text{ kg ha}^{-1}$) and low ($<1000 \text{ kg ha}^{-1}$) biomass for (A) wheat, (B) triticale, and (C) cereal rye. Sentinel-2 bands are labeled in each panel.

Finally, we examined the relationship between handheld soil moisture collections and SAR metrics. The results showed unexpectedly poor relationships ($R^2 = 0-0.08$) between soil moisture and backscatter intensities, polarimetric parameters, and InSAR coherence (Appendix A). Hence, we did not further employ remote sensing estimates of soil moisture in our analyses due to the high uncertainty in calibration.

3.1. Optical Index Results

Log-linear models best met regression assumptions and performed similarly to polynomial and segmented models. Thus, we only present results from log-linear models in the main text. Among all the considered VIs, NDVI_RE1 proved to be best at predicting cover crop biomass ($R^2 = 0.61$; RMSE = 1019; MAE = 639; AICw = 0.98; Table 3; Figure 5). Although NDRE and NDWI1 had similar coefficients of determination and error values (Table 3), their AICc were $\geq +8$ when compared to NDVI_RE1. Our findings were further supported by AICw values, where we found a 98% probability that the model using NDVI_RE1 to predict cover crop biomass was the best when compared to the other VIs included in our evaluation.

Table 3. Results of log-linear regression models predicting cover crop aboveground biomass, including the coefficient of determination (adjusted R^2), root mean square error (RMSE), and the mean absolute error (MAE), and model fit statistics—Akaike’s information criterion for small sample sizes (AICc) and AIC weights (AICw). Refer to Table 1 for optical index abbreviations. Log-linear models best met parametric assumptions. The red-edge normalized difference vegetation index with band 5 (NDVI_RE1) best estimated winter cover crop biomass.

Index	Adj R^2	RMSE	MAE	AICc	AICw
NDVI_RE1	0.61	1018.88	639.17	1337	0.98
NDWI1	0.61	1023.94	633.8	1345	0.02
NDRE	0.59	1057.69	663.15	1377	0
NDWI2	0.58	2016.30	1365.50	1389	0
NDVI	0.56	1094.22	688.71	1417	0
kNDVI	0.55	1084.84	691.23	1423	0
EVI	0.55	1079.55	686.63	1430	0
VARI_RE3	0.54	1092.24	695.93	1435	0
RTVI1	0.53	1129.64	706.84	1444	0
SR_RE1	0.53	2188.32	899.93	1452	0
RER	0.52	1486.36	770.53	1456	0
TVI	0.52	1127.99	718.22	1459	0
VARI_RE2	0.51	1142.31	732.25	1472	0
MCARI2	0.51	1207.53	755.54	1473	0
MTVI2	0.51	1207.53	755.54	1473	0
VARI_G	0.51	1101.29	700.12	1476	0
SAVI	0.5	1181.99	760.99	1487	0
NIRv	0.47	1227.51	787.64	1517	0
RTVI2	0.46	1357.68	751.95	1531	0
SR_WI	0.39	1248.93	782.68	1597	0
SR	0.36	1404.49	1750.84	1625	0
SR_RE2	0.34	1151.29	745.82	1640	0
NDVI_RE2	0.34	1135.56	737.49	1644	0
VARI_RE1	0.23	1486.54	959.25	1729	0
RTVI3	0.19	1535.50	993.11	1759	0
SR_RE3	0.14	1560.12	997.26	1796	0
NDVI_RE3	0.14	1562.67	999.44	1797	0

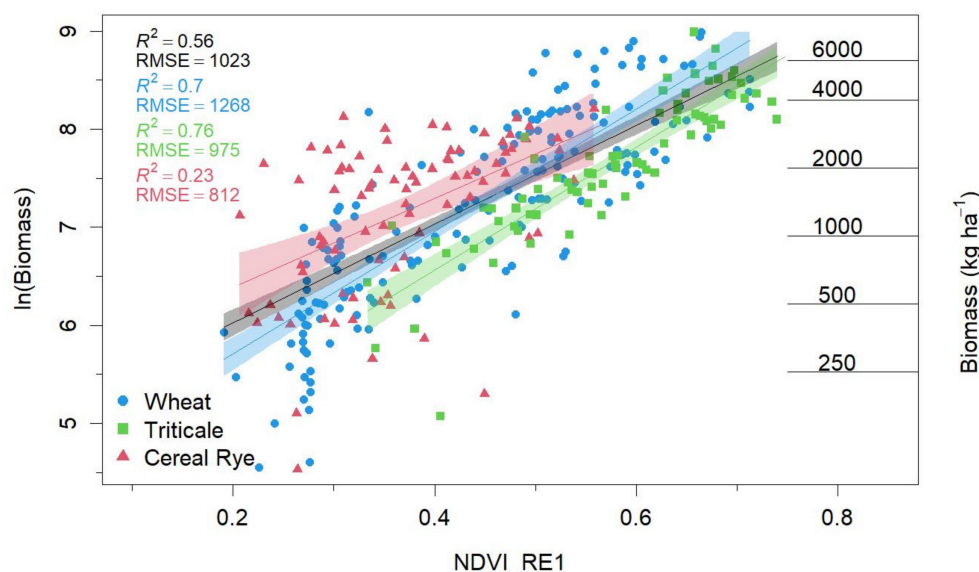


Figure 5. The natural log of cover crop biomass plotted against the normalized difference red-edge index (NDVI_RE1), which is calculated as $\frac{(B8A-B5)}{(B8A+B5)}$, where B5 is the 5th band of the Sentinel-2 satellite (the first red edge band) and the narrow band near-infrared band (B8A). Only spring data are displayed (March–May). Model fits and errors are supplied in the upper left for the entire dataset (black) and by species. An untransformed biomass estimation is appended on the right of the figure for reference.

After identifying NDVI_RE1 as most suitable for estimating cover crop biomass, we evaluated whether seasonal- or species-level differences were present using ANOVAs and slope and intercept contrasts. We found that significant effects (i.e., a relationship between NDVI_RE1 vs. biomass) varied between winter (October–February) and spring (March–May) samples (Appendix B; Table A1). Therefore, we opted to move forward with modeling the relationship between cover crop biomass and NDVI_RE1 with only spring data ($n = 332$; Figure 5), as there were only two observations in winter that exceeded 1500 kg ha^{-1} , which is the existing saturation point identified for cereal grass cover crops [14]. Furthermore, we found species-level differences between cereal rye, triticale, and wheat (Appendix B; Table A2). In our study, cereal rye had lower observed biomass ranges than triticale and wheat. Therefore, we further examined whether these species-level differences remained when we limited our analysis to similar biomass ranges for these three cereal grass species. Our results suggest that species-level differences were still present within this sub-analysis (results not shown). Therefore, as we found significant differences between species (primarily between cereal rye and the other two species) in our ANOVAs and slope-intercept contrasts, we also modeled species separately (Figure 5). With these season*species interactions, the results of our optical index selection (NDVI_RE1) showed substantial increases in goodness-of-fit wheat ($R^2 = 0.70$) and triticale ($R^2 = 0.76$). However, we observed that the relationship between NDVI_RE1 and cereal rye biomass performed poorly ($R^2 = 0.23$).

3.2. Optical—Synthetic Aperture Radar (SAR) Results

Results from objective 1 indicated that NDVI_RE1 was our best-performing optical index, but also that seasonal and species level effects were present in our data. Therefore, our analyses integrating optical and SAR data focused solely on spring samples ($n = 332$) and modeled species separately in objective 2. Each SAR metric (backscatter intensities and indices, polarimetric parameters, and InSAR coherence) was individually added to NDVI_RE1 regression models to predict cover crop biomass and assess how model statistics changed with each additional SAR metric.

The addition of most SAR metrics did not substantially improve model fits or reduce errors compared to models that had only NDVI_RE1 (Table 4) but were species-specific. However, combining InSAR coherence and NDVI_RE1 did increase our ability to predict the biomass of all three cereal grass species (Table 4), with improved model fits (i.e., R^2 increased by 4 to 11% and AICc decreased by 15 to 24 among species). Wheat, triticale, and cereal rye models with InSAR coherence also demonstrated reductions in error that ranged from small to moderate: RMSE decreased by 42, 182, and 36 kg ha⁻¹ and MAE decreased by 95, 84, and 52 kg ha⁻¹, respectively.

Table 4. Results of combined optical and synthetic aperture radar (SAR) species-specific regression models. Models combined the optical normalized difference red-edge index using band 5 (NDVI_RE1) with SAR backscatter indices (vertical-vertical (VV), vertical-horizontal (VH), VH/VV, and radar vegetation index (RVI)) and polarimetric parameters (alpha, entropy (H), anisotropy (A), InSAR coherence (Coh)), sequentially. Models were evaluated using goodness of fit (adjusted R^2), root mean square error (RMSE), mean absolute error (MAE), and model fit statistics—Akaike’s information criterion for small samples (AICc) and AIC weights (AICw).

Model	Adj R^2	RMSE	MAE	AICc	AICw
Wheat					
NDVI_RE1 + Coh + H	0.74	1223.24	770.73	258	0.63
NDVI_RE1 + Coh	0.74	1226.79	783.74	259	0.37
NDVI_RE1 + H	0.71	1263.33	848.04	280	0
NDVI_RE1 + VH	0.70	1285.51	872.42	281	0
NDVI_RE1 + A	0.70	1280.42	853.11	281	0
NDVI_RE1 + Alpha	0.70	1273.26	854.26	282	0
NDVI_RE1	0.70	1268.34	865.56	282	0
NDVI_RE1 + RVI	0.70	1278.49	870.41	282	0
NDVI_RE1 + VHVV	0.70	1273.13	866.04	283	0
NDVI_RE1 + VV	0.70	1267.58	865.75	284	0
Triticale					
NDVI_RE1 + Coh	0.81	792.95	553.09	46	0.72
NDVI_RE1 + Coh + A	0.81	783.8	542.96	48	0.28
NDVI_RE1 + A	0.77	924.37	618.7	59	0
NDVI_RE1 + H	0.77	934.07	621.4	60	0
NDVI_RE1 + Alpha	0.77	933.43	623.29	61	0
NDVI_RE1 + VHVV	0.77	957.74	627.05	61	0
NDVI_RE1	0.76	974.67	637.5	61	0
NDVI_RE1 + RVI	0.76	904.44	618.24	62	0
NDVI_RE1 + VH	0.76	954.15	634.29	63	0
NDVI_RE1 + VV	0.76	980.84	638.24	63	0
Cereal Rye					
NDVI_RE1 + VV + RVI + Coh	0.38	771.81	596.63	165	0.75
NDVI_RE1 + Coh	0.34	775.54	590.93	167	0.24
NDVI_RE1 + VV	0.28	803.22	636.09	175	0
NDVI_RE1 + RVI	0.25	836.67	653.54	178	0
NDVI_RE1 + VH	0.25	800.37	638.94	178	0
NDVI_RE1	0.23	811.92	643.24	180	0
NDVI_RE1 + H	0.22	811.37	637.39	181	0
NDVI_RE1 + VHVV	0.23	811.87	641.96	181	0
NDVI_RE1 + Alpha	0.22	815.53	641.43	182	0
NDVI_RE1 + A	0.22	813.57	640.74	182	0

Models including both NDVI_RE1 and InSAR coherence were significantly better than the model using NDVI_RE1 alone in all three species ($F = 15.75\text{--}26.86$, $p < 0.001$; Table 5). Similarly, models with both NDVI_RE1 and InSAR coherence demonstrated an increased predictive ability in terms of cross-validation compared to models with just NDVI_RE1

($\Delta R^2 = +3\text{--}9\%$; Table 6). We also observed small-to-moderate reductions in errors in wheat, triticale, and rye cross-validation ($\Delta \text{RMSE} = 37, 188, \text{ and } 23 \text{ kg ha}^{-1}$; $\Delta \text{MAE} = 74, 92, \text{ and } 37 \text{ kg ha}^{-1}$, respectively).

Table 5. Results of combined optical and synthetic aperture radar (SAR) species-specific analysis of variance (ANOVA) models. Models combined the normalized difference red-edge index using band 5 (NDVI_RE1) optical index and SAR backscatter indices and polarimetric parameters. All models are compared to the NDVI_RE1 model with no SAR metrics to evaluate statistically significant improvements when SAR metrics are included. Combined models varied by species, and all significant combined models included InSAR coherence (Coh). Wheat also included entropy (H); triticale also included anisotropy (A); and cereal rye included vertical-vertical polarization (VV) and the radar vegetation index (RVI).

ANOVA F-Values									
Model	VV	VH	VHV	RVI	Alpha	A	H	Coh	Combined
Wheat	0.08	2.59	0.92	1.99	1.9	2.51	3.64 *	26.86 ***	15.17 ***
Triticale	0.2	0.5	2.23	1.67	2.81	4.72 *	3.85 *	18.64 ***	9.43 ***
Cereal Rye	6.87 **	3.46	1.22	4.00 *	0.23	0.3	0.75	15.75 ***	7.80 ***

* $p < 0.05$, ** $p < 0.01$, *** $p < 0.001$.

Table 6. Results of combined optical and synthetic aperture radar (SAR) analysis of variance cross-validation. Models combined the normalized difference red-edge index using band 5 (NDVI_RE1) optical index and the best SAR metrics—InSAR coherence (Coh), entropy (H), anisotropy (A), vertical-vertical backscatter (VV), and the radar vegetation index (RVI). We split the data into 70% train and 30% test splits to estimate goodness of fit (adjusted R^2) and error (RMSE, MAE). We iterated these splits 100 times and reported the mean statistics.

Model	Mean R^2	Mean RMSE	Mean MAE
Wheat			
NDVI_RE1	0.71	1280.97	879.3
NDVI_RE1 + Coh	0.74	1243.94	805.26
NDVI_RE1 + Coh + H	0.74	1246.88	789.74
Triticale			
NDVI_RE1	0.77	1013.39	686.37
NDVI_RE1 + Coh	0.82	825.34	593.98
NDVI_RE1 + Coh + A	0.81	827.47	591.86
Cereal Rye			
NDVI_RE1	0.24	826.94	662.69
NDVI_RE1 + Coh	0.33	804.32	625.82
NDVI_RE1 + VV + RVI + Coh	0.34	905.43	693.12

We observed that, as biomass increased, InSAR coherence decreased, a pattern that results from increased volume scattering producing return signals with a random phase (Figure 6). However, in 47 out of 573 datapoints (i.e., two April sampling dates: cereal rye = 0, triticale = 26, wheat = 21), cover crop termination events occurred between the acquisition of the InSAR image pairs. Termination events may result in additional InSAR coherence decreases as they significantly alter the landscape structure between images in the InSAR pair. For this reason, we performed a sensitivity analysis to assess whether model statistics changed between models with or without including these 47 observations and found no substantial differences (Appendix C).

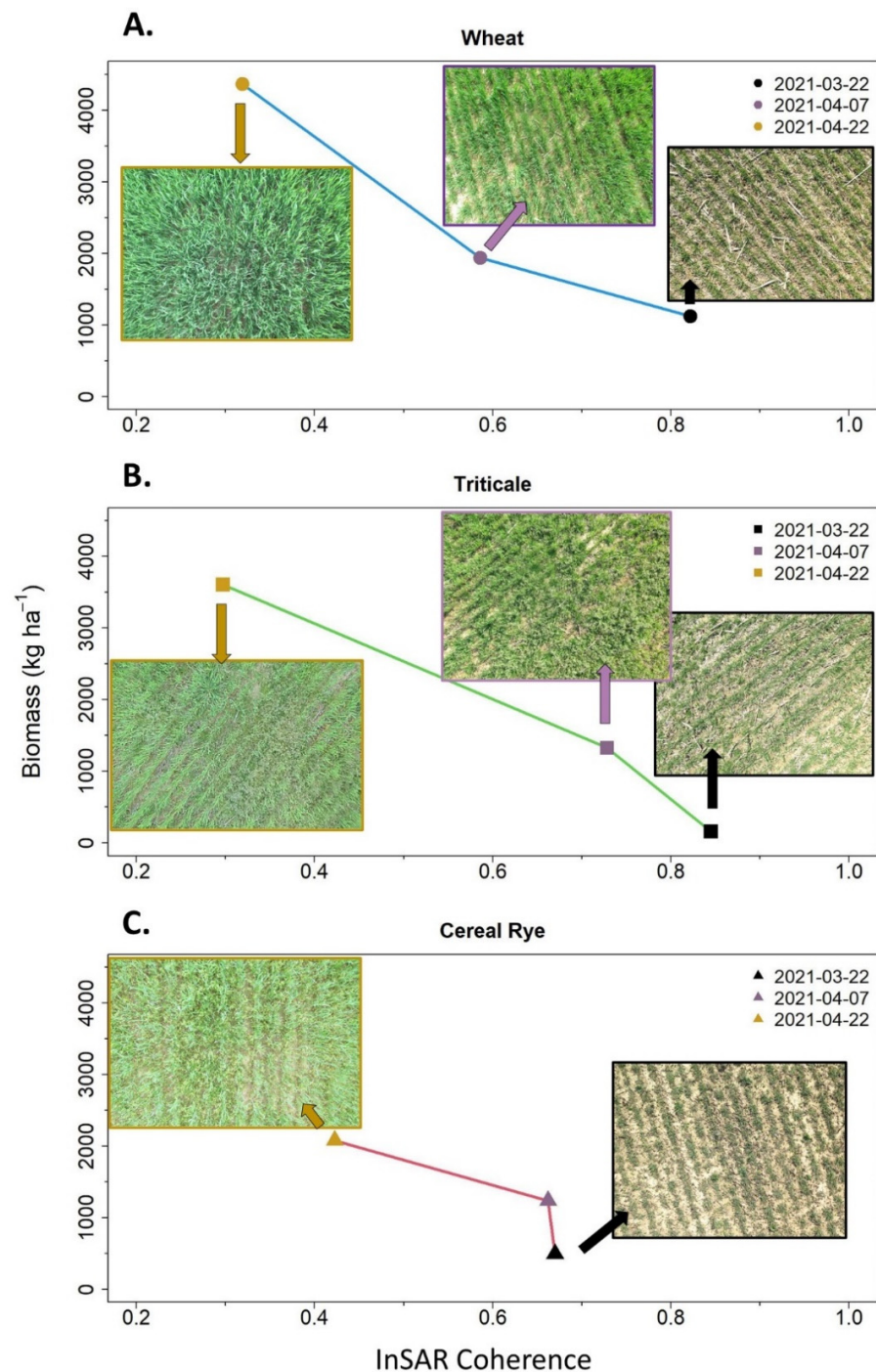


Figure 6. Examples of wheat (A), triticale (B), and cereal rye (C), biomass plotted against InSAR coherence. Lower InSAR coherence values are indicative of general changes in field conditions between two images forming an InSAR pair as well as general shifts from coherent surface scattering to incoherent random scattering as cover crops mature comparing different InSAR pairs. For the biomass sampling dates (included in the upper right of each panel) the following InSAR pairs were matched: (1) 3-14-21 and 3-26-21, (2) 3-26-21 and 4-19-21, and (3) 4-19-21 and 5-1-21. For these example fields, termination occurred on 5-27-21 for cereal rye, 4-29-21 for triticale, and 6-28-21 for wheat.

As the addition of multiple SAR metrics produced statistically improved biomass predictions compared to models with NDVI_RE1 alone (Table 5), we also explored the use of multiple SAR parameters in addition to NDVI_RE1 for each of the three cover crop

species, which we refer to as “combined models.” All combined models were screened for collinearity and no predictor variables correlated above the predefined threshold ($r > 0.7$). For wheat and triticale, the best-performing combined model contained NDVI_RE1, InSAR coherence, and entropy (wheat) or anisotropy (triticale) as predictor variables based on a combination of R^2 , error measures, AICc and AICw (Tables 3 and 5). In contrast, the best-performing model for the prediction of cereal rye biomass included NDVI_RE1, InSAR coherence, as well as VV and RVI derived from backscatter intensities ($\Delta R^2 = +15\%$; Table 4). Despite these gains in SAR metrics in the cereal rye models, they remained the poorest-performing models compared to wheat and triticale. Combined models for each of the three species were also statistically more significant than models with NDVI_RE1 alone (Table 5), but not when compared to models that included only InSAR coherence and NDVI_RE1 except for cereal rye (not shown). Similarly, we found no substantial changes between combined models and those with NDVI_RE1 and InSAR coherence alone during cross-validation (Table 6).

4. Discussion

4.1. Normalized Difference Red-Edge Index Best Predicts Cover Crop Biomass

Our results indicate that the best VI for measuring the aboveground biomass of cereal grass cover crop species is the normalized difference vegetation index calculated using Sentinel-2 red-edge band 5 (NDVI_RE1), supporting our first hypothesis regarding the utility of the red-edge region for the improved biomass estimation of winter cover crops. Our findings are consistent with other studies that observed that the red-edge region was important for estimating crop biophysical characteristics, including LAI, the fraction of absorbed photosynthetically active radiation, fraction of vegetation cover, and biomass [17,19,25,28,29]. The red-edge region is a unique characteristic of healthy vegetation as it links the highly absorptive red region, which is sensitive to chlorophyll, and the highly reflective NIR region, which is linked to plant internal cellular structure [20,76]. We found that band 5 (centered at 704 nm, 690–720 nm in the red-edge region) was most important for cover crop biomass estimation; the VIs containing band 5 consistently outperformed those from the middle red-edge (band 6, 733–747 nm) and the latter red-edge (band 7, 770–790 nm) region (Table 3). Despite this, we still observed NDVI_RE saturation at $\sim 1900 \text{ kg ha}^{-1}$ ($\sim 27\%$ of our samples), which is similar to, although slightly higher than, previous thresholds observed for NDVI in cereal grass cover crops [14]. This finding may, in part, be because the index is normalized and is, therefore, bounded -1 to $+1$, or because a reflectance below 720 nm is not strongly influenced by leaf layering when compared to a reflectance greater than 725 nm [76], indicating that shorter red-edge wavelengths are more likely to experience a saturation effect compared to longer red-edge wavelengths. Therefore, it appears that the shorter red-edge region is still sensitive to chlorophyll concentrations (up to $\sim 705 \text{ nm}$) [77] but not as absorptive as the red region and is, therefore, slower to saturate as biomass increases. While our study focused on cover crops, our findings regarding the utility of NDVI_RE1 may be useful for future work dealing with the saturation of VIs in other contexts or for cereal grasses in other agricultural regions that are grown as commodity crops, although recalibration would be required for different species and regions.

We also examined whether biomass–VI relationships varied seasonally (winter–spring) and relative to species. As expected, winter and spring relationships varied significantly (Appendix B), in accordance with other studies [14,78]. Biologically, we anticipated this finding because cover crop growth is halted during the winter dormancy and plants experience chlorosis or yellowing of leaves due to frost damage. This results in biomass that is less detectable by vegetation indices, and the plants later recover their reflectance following spring green-up.

We also observed significant species-level differences (Appendix B). Previous work on cash crops has shown that the relationship between VIs and biophysical characteristics, including chlorophyll content, LAI, and leaf inclination angle, are species-specific [79,80]. Previous work also noted that the performance of VIs (NDVI and a red-edge index) to

predict cover crop biomass estimations were species-dependent [17]. It should be noted that our cereal rye samples—which showed the most pronounced difference in slope and intercept from the other two species—may not be entirely representative of cereal rye broadly, because we observed patchy growth in several cereal rye fields included in this study. While we acknowledge the limitations of the present study, our results were consistent with other studies that have observed significant species-level differences in the NDVI biomass relationships among cereal grass species on a larger scale [78], possibly due to differences in growth form and leaf angle distribution. Species-level differences in growth pattern among cereal rye, wheat, and triticale were somewhat visually evident in nadir photographs (Figure 3). For instance, triticale appeared to have more ground cover earlier than wheat and cereal rye, due to a more prostrate growth habit, while cereal rye appeared to be taller and possess a more erect leaf angle distribution in the spring. Based on these findings, future research could investigate whether species-level differences in canopy architecture, such as leaf angle distribution, are truly present among cereal grass cover crops and how this may influence the remote sensing of biomass. Such parameters may play an important role in light scattering [81] and will, therefore, influence optical remote sensing observations.

4.2. Interferometric Synthetic Aperture Radar (InSAR) Coherence Improved Cover Crop Biomass Estimates, but Did Not Improve Issues with Saturation at High Biomass Levels

We assessed whether the integration of optical and SAR metrics would improve our ability to estimate cover crop biomass, specifically past optical saturation. We consistently observed improved fits and predictive ability in our models when both InSAR coherence and NDVI_RE1 were included as predictors (Tables 4–6), but the magnitude of improvement varied by species (R^2 increase of 4–11%). Despite the improved model performance found with the addition of InSAR coherence, we did not observe improved predictions of cover crop biomass at high biomass levels ($>2000 \text{ kg ha}^{-1}$). Although InSAR coherence has not previously been used to predict biomass, other studies demonstrated the utility of InSAR coherence for estimating cash crop height [46,47] and growth [48]. InSAR coherence remains moderate to high (~ 0.5 – 1) when crop growth is slow or otherwise limited—such as during the winter dormancy period for cover crops—but will decrease as crop growth continues [82]—such as during the spring growth period when cover crops rapidly accumulate large quantities of biomass (Figure 6). However, InSAR coherence is also sensitive to other changes in scene texture and composition for agricultural regions such as tillage, soil moisture variations, and harvesting, as these events also cause a significant change in return signal phase. The use of InSAR coherence for the biomass estimation of cereal grass cover crops, in combination with the NDVI_RE1 optical index, performed best in this study, provided that one is aware of management activities such as cover crop termination, as such events will also show similarly low coherence values to those of growing vegetation. If management information is not easily obtainable from growers, future work could consider pairing VIs to differentiate termination from a green field, or employing the within-season termination (WIST) algorithm, which has shown a strong ability to estimate cover crop termination dates [11].

In addition to InSAR coherence, we also found species-specific differences between other SAR metrics. Incorporating polarimetric parameters such as entropy and anisotropy, respectively, along with NDVI_RE1 and InSAR coherence, resulted in better wheat and triticale biomass predictive models compared to use of the optical model alone. However, neither entropy nor anisotropy aided in better predictions past the point of saturation and also appeared to saturate at a similar biomass level to NDVI_RE1 ($\sim 1900 \text{ kg ha}^{-1}$). This may be, in part, because we performed polarimetric decompositions on Sentinel-1 dual-pol imagery with VV and VH channels only, as opposed to quad-pol imagery. Previous work demonstrated that alpha, entropy, and anisotropy estimated winter wheat biomass moderately well ($R^2 = 0.51, 0.42, \text{ and } 0.44$, respectively) using RADARSAT-2 quad-pol imagery, which more effectively resolves target-scattering mechanisms when compared to dual-pol

SAR imagery [83]. Despite the noted model improvements in wheat and triticale biomass predictive models with the inclusion of entropy and anisotropy in this study, we observed no substantial differences when compared to the model with only InSAR coherence and NDVI_RE1 for both wheat ($\Delta R^2 = 0$; $\Delta RMSE = +3 \text{ kg ha}^{-1}$; $\Delta MAE = -15 \text{ kg ha}^{-1}$) and triticale ($\Delta R^2 = 0\%$; $\Delta RMSE = +2 \text{ kg ha}^{-1}$; $\Delta MAE = +2 \text{ kg ha}^{-1}$) during cross-validation. Future work could investigate the efficacy of cover crop biomass estimations using the quad-pol polarimetric decompositions applied to imagery acquired from satellites such as RADARSAT-2, although the data are not publicly available as with Sentinel-1. Improvements in polarimetric decompositions could also be achieved by using dual-pol imagery with both linear co-polarizations (HH and VV) [83]. The compact polarimetry operating modes of RADARSAT-2 and the RADARSAT Constellation Mission (RCM)—with a circular polarization transmitted signal and V and H linear receivers—would likely lead to substantial improvements in the accuracy of polarimetric decomposition parameters compared to linear dual-pol operating modes. The compact polarimetry mode is similarly effective as a quad-pol for crop classifications [84], indicating potential performance similarities for crop biomass estimation.

Optical-SAR models for cereal rye differed from wheat and triticale in that model performance improved when backscatter intensities (VV, VH, and RVI) were included (Tables 3 and 4). Previous work demonstrated a significant relationship between cross-polarization (VH) backscatter and biomass [39], as complex canopies are more likely to volume scatter SAR signals, leading to higher VH backscatter values. However, others found that the VV and HH backscatter were correlated with the biomass of canola (*Brassica napus*) and corn, respectively, which is likely indicative of non-volume (i.e., single bounce, double bounce) scattering interactions with well-defined crop structures (horizontal and broad canola leaves (*Brassica napus*), and vertical corn stalks) [43]. In this study, however, we would expect a greater volume scattering (VH) response for cereal grass canopies with smaller and less geometrically well-defined structures, but with potential for variability between species with slightly different canopy structures. If our supposition regarding species-level canopy geometry differences is accurate, and cereal rye shows a more erect leaf angle distribution, we would expect cereal rye to exhibit a relatively higher VV than VH when compared to the other species, which exhibit more volume scattering in canopies with less well-defined structures. These differences in canopy-scattering mechanisms between species may indeed be present in our results, as indicated by the fact that including RVI (fundamentally a VV and VH comparison metric) only improved the performance of the cereal rye biomass predictive model, which is consistent with previous work on cash crops [85]. The best-performing biomass predictive model for cereal rye included NDVI_RE1, InSAR coherence, VV backscatter, and RVI. This combined model provided the largest increase in its predictive ability and the highest AICw ($\Delta R^2 = +15\%$; $AICw = 0.75$). However, as with wheat and triticale, cross-validation indicated that the combined cereal rye model does not outperform the optical model with InSAR coherence alone (Table 6).

Although we found species-specific responses to Sentinel-1 C-band SAR backscatter and polarimetric parameters, InSAR coherence consistently improved models for all species both during model evaluation (Table 4) and cross-validation (Table 6). Therefore, for Sentinel-1 C-band SAR operating in dual-pol mode, we conclude InSAR coherence layers were the most effective in improving cover crop biomass predictions when combined with NDVI_RE1. InSAR coherence layers generated using Gamma software are now also present in ASF's more generalized VERTEX platform (in addition to the HyP3 tool used in this study) [71]. ASF's cloud-based SAR processing tools were critical to this study, as InSAR processing would likely be prohibitively cost-, time-, and computer resource-intensive for a local machine. ASF capabilities will likely be critical to the processing of imagery from the upcoming NASA-ISRO SAR (NISAR) mission operating at L-band and S-band wavelengths which is slated to acquire an unprecedented volume of satellite imagery on a daily basis. With relevance to the NISAR mission, the suitability of L-band SAR data to estimate cover crop biomass could be evaluated, as previous work demonstrated their

efficacy in estimating crop biomass and LAI [40,43]. Further the dual-frequency and greater polarimetric capabilities of NISAR will likely provide opportunities for cover crop biomass characterization with SAR imagery that are well beyond what was possible in this study.

4.3. Soil Moisture and Biomass Were Poorly Related to Synthetic Aperture Radar (SAR) Metrics

We examined the relationship between Sentinel-1 SAR metrics and soil VWC, as SAR signals are sensitive to soil moisture, but found no significant relationship between VWC and all SAR metrics examined in this analysis (Appendix A). This may be because Sentinel-1 operates at a C-band frequency, which may be more responsive to crop conditions than soil moisture, with two notable studies finding that C-band SAR VV backscatter decreases in response to increasing winter wheat stem height, while soil moisture has less of an impact on backscatter [86,87]. However, when examined independently, both VV and VH backscatter intensities also showed very poor relationships with cover crop biomass (Appendix D), which is surprising, as shallower incident angles (further off nadir) have been associated with the effective estimation of wheat biomass [41,88]. Others also demonstrated that C-band SAR failed to detect soil moisture when NDVI exceeded 0.7 [88]. In our study, the use of SAR metrics focused on the spring period (March–May), when we observed high biomass levels, and approximately half of our spring observations had NDVI values greater than 0.7 which likely influenced the relationship between in situ soil moisture measurements and SAR metrics. For samples with an NDVI less than 0.70, it was likely that the combined influence of background soil variability and variability in attenuating structures (small diameter vertical stem growth) [86,89] culminated in combined backscatter values that could not be related back to either factor in isolation. The ability to interpret and statistically isolate these factors becomes even more challenging when considering factors such as surface roughness, crop residue presence, and crop residue moisture content, all of which influence total backscatter intensity in a given image pixel.

5. Conclusions

Estimating cover crop performance is important in quantifying ecosystem services, yet few works to date have evaluated remote sensing approaches to characterize cover crop performance across the landscape. The results from our study demonstrated that estimating cover crop biomass is feasible using VIs alone, as well as by integrating optical and SAR remote sensing, but that season- and species-level effects were also present. We found that the normalized difference red-edge index Sentinel-2 with band five (NDVI_RE1) and Sentinel-1 InSAR coherence provided the best predictions of cereal grass cover crop biomass. These findings may broadly support conservation efforts in the Chesapeake Bay region, which focus on incentivizing cereal grass cover crops and mixes as they decrease nutrient flow into local waterways, which may help to address the 2030 United Nations Sustainable Development Goal to “ensure availability and sustainable management of water and sanitation for all.” However, further research is needed to enhance the prediction of higher biomass levels ($>1900 \text{ kg ha}^{-1}$), which SAR metrics were ineffective at improving based on the predictive capacity of NDVI_RE1 alone. To address this continued concern, future work could consider the combination of weather and climate variables, machine learning algorithms, integration of proximal sensing and satellite observations, as well as the integration of process-based crop-soil simulation models and remote sensing observations.

Author Contributions: Conceptualization, J.S.J., B.T.L., W.D.H., S.B.M., A.T. and R.T.; methodology, J.S.J., B.T.L., W.D.H., S.B.M., A.T. and A.G.; software, J.S.J. and B.T.L.; validation, J.S.J.; formal analysis, J.S.J.; investigation, J.S.J., B.T.L., W.D.H., S.B.M., A.T. and R.T.; resources, S.B.M., W.D.H.; data curation, J.S.J., B.T.L., A.T., A.G.; writing—original draft preparation, J.S.J. and B.T.L.; writing—review and editing, J.S.J., B.T.L., W.D.H., S.B.M., A.T., R.T. and A.G.; visualization J.S.J. and A.G.; supervision, W.D.H. and S.B.M.; project administration, S.B.M. and W.D.H.; funding acquisition, S.B.M. and W.D.H. All authors have read and agreed to the published version of the manuscript.

Funding: This project was supported by the U.S. Geological Survey Land Change Science Program within the Land Resources Mission Area; the U.S. Department of Agriculture—Agricultural Research Service, National Program 211; and the U.S. Department of Agriculture Lower Chesapeake Long Term Agricultural Research (LTAR) program. Additionally, this work is supported by the Agriculture and Food Research Initiative’s Sustainable Agricultural Systems Coordinated Agricultural Project [award no. 2019-68012-29818] and Water Coordinated Agricultural Project [award no. 2018-68011-28372] from the United States Department of Agriculture (USDA) National Institute of Food and Agriculture.

Data Availability Statement: Data supporting this analysis are published and available for download [55].

Acknowledgments: Any use of trade, firm, or product names is for descriptive purposes only and does not imply endorsement by the U.S. Government.

Conflicts of Interest: The authors declare no conflict of interest.

Appendix A

Soil Moisture relationships over time and with synthetic aperture radar (SAR) backscatter intensities, polarimetric parameters, and interferometric SAR (InSAR) coherence.

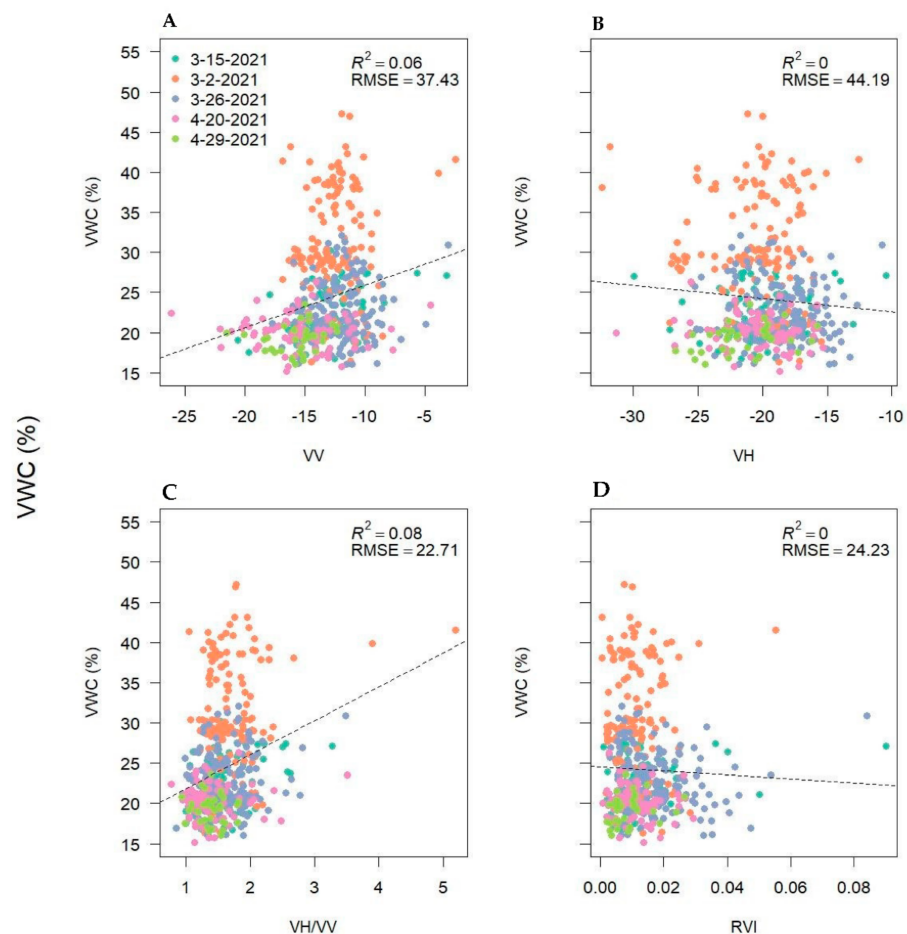


Figure A1. Volumetric water content (VWC) as a function of synthetic aperture radar linear backscatter intensities—vertical-vertical (VV; **A**), vertical horizontal (VH, **B**), VV/VH ratio (**C**) and the radar vegetation index (RVI; **D**)—from five handheld soil moisture data collections in March and April adjacent to plot locations and across the seven study fields. VWC collections were timed with Sentinel-1 overpasses.

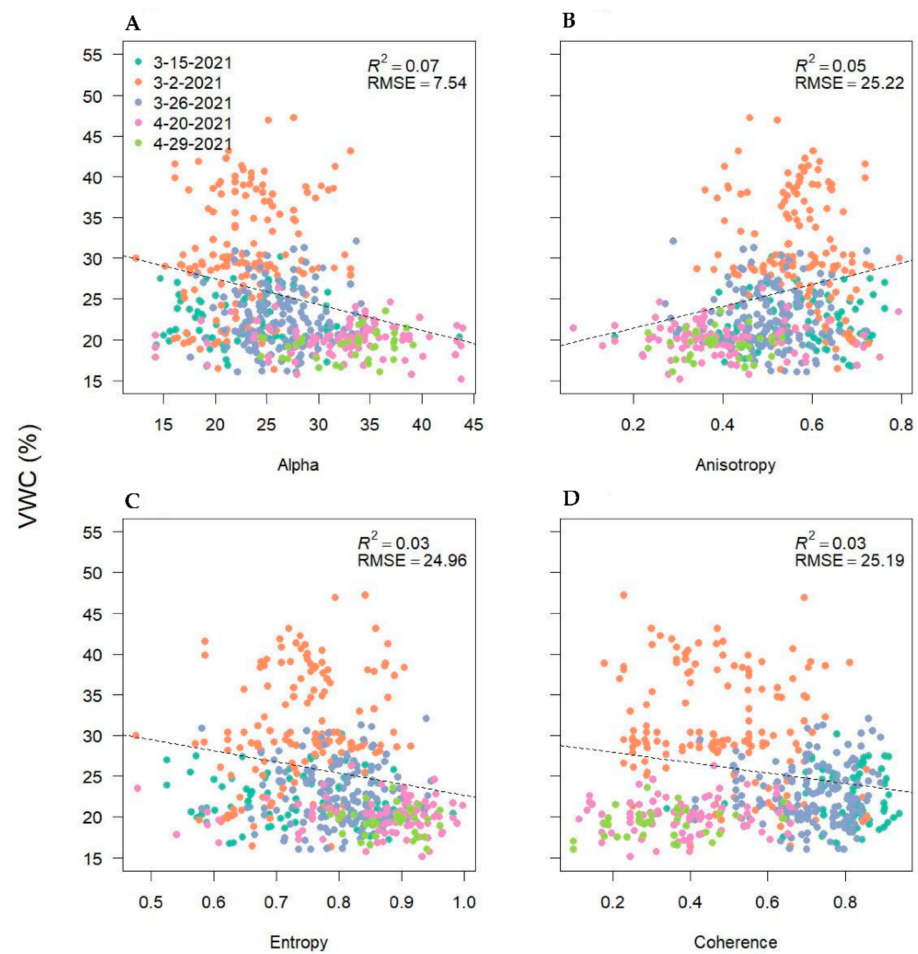


Figure A2. Volumetric water content (VWC) as a function of synthetic aperture radar polarimetric decompositions (alpha angle—(A); anisotropy—(B); entropy—(C)) and interferometric (InSAR) coherence (D) from five soil moisture data collections in March and April adjacent to plot locations and across the seven study fields. VWC collections were timed with Sentinel-1 overpasses.

Appendix B

Results of analysis of variance (ANOVA), slope and intercept contrasts with the normalized difference red-edge index with band 5 (NDVI_RE1) and season (A.) and species (B.) in spring.

Table A1. Season contrast.

ANOVA				
	DF	Sum Squares	Mean Square	F Value
NDVI_RE1	1	544.10	544.10	1294.70 ***
Season	1	102.80	102.80	244.60 ***
Residuals	570	239.50	0.4	
Slope and Intercept Contrasts				
	DF	Estimate	SE	T Ratio
Spring v. Winter (slope)	569	−1.07	0.26	−2.31 *
0 Spring v. 0 Winter (intercept)	569	1.36	0.18	7.56 ***

$p < 0.05$ *, $p < 0.001$ ***.

Table A2. Species contrasts in spring.

ANOVA				
	DF	Sum Squares	Mean Square	F Value
NDVI_RE1	1	153.98	153.98	510.25 ***
Species	2	15.71	7.85	26.02 ***
Residuals	328	98.98	0.30	
Slope and Intercept Contrasts				
	DF	Estimate	SE	T Ratio
Rye v. Triticale (slope)	326	−1.73	0.96	−1.81
Rye v. Wheat (slope)	326	−1.71	0.78	−2.18 *
Triticale v. Wheat (slope)	326	0.02	0.71	0.03
0 Rye v. 0 Triticale (intercept)	326	1.43	0.46	3.12 **
0 Rye v. 0 Wheat (intercept)	326	1.02	0.31	3.32 **
0 Triticale v. 0 Wheat (intercept)	326	−0.41	0.40	−1.03

$p < 0.10$, $p < 0.05$ *, $p < 0.01$ **, $p < 0.001$ ***.

Appendix C

Table A3. Optical SAR results by species that removed 47 observations that experienced a termination event between InSAR pairs. Results do not vary substantially from original model results. No cereal rye models are presented because all termination dates occurred after In-SAR pairs. Species contrasts in spring.

Model	Adj R ²	RMSE	MAE
Wheat			
NDVI_RE1+ Coh + H	0.74	1180.84	745.22
NDVI_RE1+ Coh	0.74	1189.03	758.38
Triticale			
NDVI_RE1+ Coh	0.82	876.14	611.33
NDVI_RE1+ Coh + A	0.82	862.59	603.02

Appendix D

Biomass relationships with synthetic aperture radar (SAR) backscatter intensities, polarimetric parameters, and interferometric SAR (InSAR) coherence.

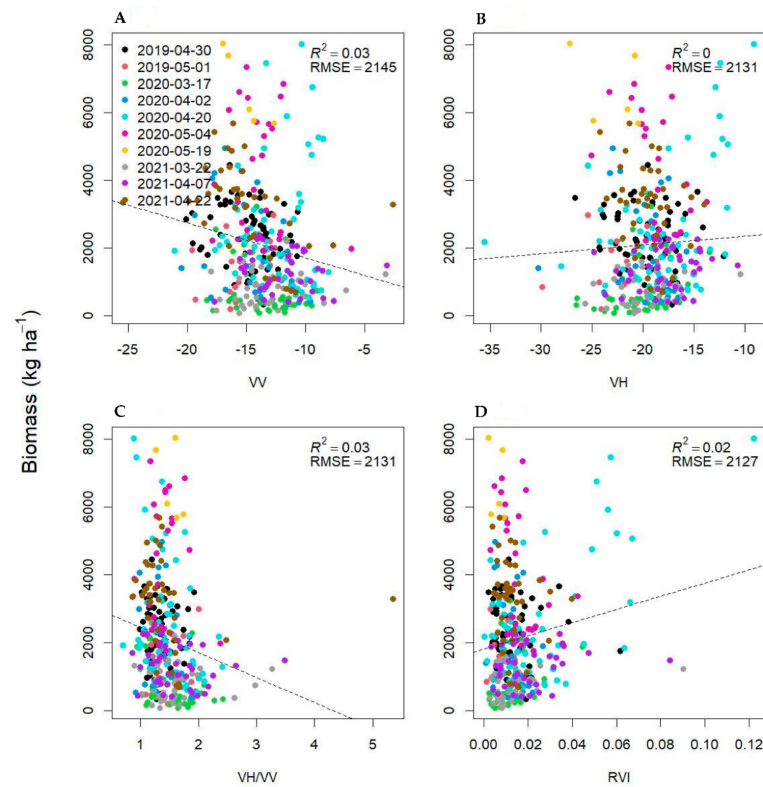


Figure A3. Cover crop biomass as a function of synthetic aperture radar linear backscatter intensities—vertical-vertical (VV; (A)), vertical horizontal (VH; (B)), VV/VH ratio (C) and the radar vegetation index (RVI; (D)).

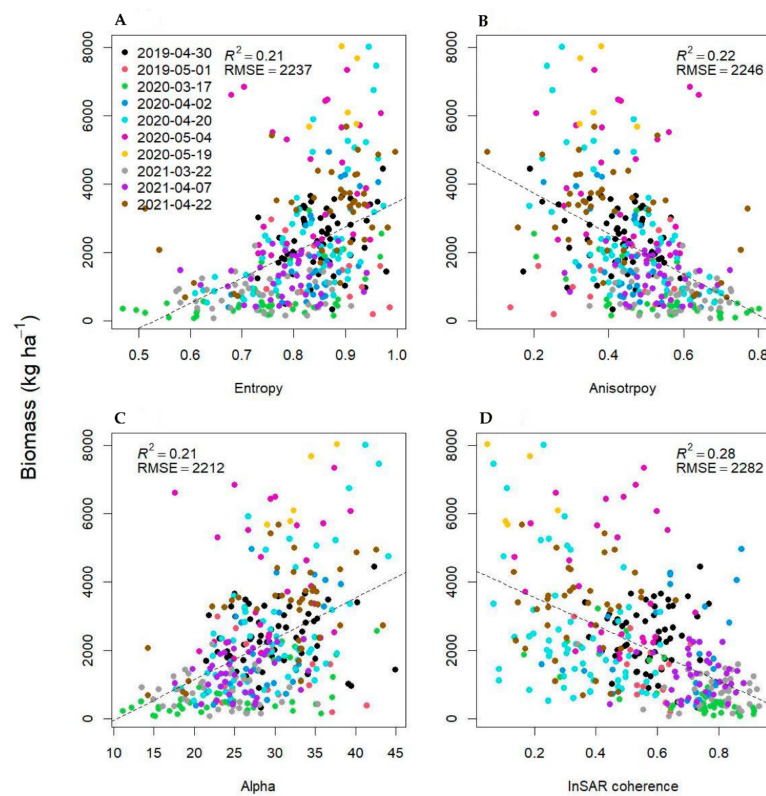


Figure A4. Biomass as a function of synthetic aperture radar polarimetric decompositions (alpha angle—(A); anisotropy—(B); entropy—(C)) and interferometric (InSAR) coherence (D).

References

1. Wallander, S.; Smith, D.; Bowman, M.; Claassen, R. *Cover Crop Trends, Programs, and Practices in the United States*; EIB 222; U.S. Department of Agriculture, Economic Research Service: Washington, DC, USA, 2021.
2. Blanco-Canqui, H.; Shaver, T.M.; Lindquist, J.L.; Shapiro, C.A.; Elmore, R.W.; Francis, C.A.; Hergert, G.W. Cover Crops and Ecosystem Services: Insights from Studies in Temperate Soils. *Agron. J.* **2015**, *107*, 2449–2474. [[CrossRef](#)]
3. Mirsky, S.B.; Ryan, M.R.; Curran, W.S.; Teasdale, J.R.; Maul, J.; Spargo, J.T.; Moyer, J.; Grantham, A.M.; Weber, D.; Way, T.R.; et al. Conservation Tillage Issues: Cover Crop-Based Organic Rotational No-till Grain Production in the Mid-Atlantic Region, USA. *Renew. Agric. Food Syst.* **2012**, *27*, 31–40. [[CrossRef](#)]
4. Thapa, R.; Mirsky, S.B.; Tully, K.L. Cover Crops Reduce Nitrate Leaching in Agroecosystems: A Global Meta-Analysis. *J. Environ. Qual.* **2018**, *47*, 1400–1411. [[CrossRef](#)] [[PubMed](#)]
5. Thapa, R.; Poffenbarger, H.; Tully, K.L.; Ackroyd, V.J.; Kramer, M.; Mirsky, S.B. Biomass Production and Nitrogen Accumulation by Hairy Vetch–Cereal Rye Mixtures: A Meta-Analysis. *Agron. J.* **2018**, *110*, 1197–1208. [[CrossRef](#)]
6. Thapa, R.; Tully, K.L.; Reberg-Horton, C.; Cabrera, M.; Davis, B.W.; Fleisher, D.; Gaskin, J.; Hitchcock, R.; Poncet, A.; Schomberg, H.H.; et al. Cover Crop Residue Decomposition in No-till Cropping Systems: Insights from Multi-State on-Farm Litter Bag Studies. *Agric. Ecosyst. Environ.* **2022**, *326*, 107823. [[CrossRef](#)]
7. Finney, D.M.; White, C.M.; Kaye, J.P. Biomass Production and Carbon/Nitrogen Ratio Influence Ecosystem Services from Cover Crop Mixtures. *Agron. J.* **2016**, *108*, 39–52. [[CrossRef](#)]
8. Hively, W.D.; Lang, M.; McCarty, G.W.; Keppler, J.; Sadeghi, A.; McConnell, L.L. Using Satellite Remote Sensing to Estimate Winter Cover Crop Nutrient Uptake Efficiency. *J. Soil Water Conserv.* **2009**, *64*, 303–313. [[CrossRef](#)]
9. Hagen, S.C.; Delgado, G.; Ingraham, P.; Cooke, I.; Emery, R.; Fisk, J.P.; Melendy, L.; Olson, T.; Patti, S.; Rubin, N.; et al. Mapping Conservation Management Practices and Outcomes in the Corn Belt Using the Operational Tillage Information System (OpTIS) and the Denitrification–Decomposition (DNDC) Model. *Land* **2020**, *9*, 408. [[CrossRef](#)]
10. Hively, W.D.; Duiker, S.; McCarty, G.; Prabhakara, K. Remote Sensing to Monitor Cover Crop Adoption in Southeastern Pennsylvania. *J. Soil Water Conserv.* **2015**, *70*, 340–352. [[CrossRef](#)]
11. Gao, F.; Anderson, M.C.; Hively, W.D. Detecting Cover Crop End-of-Season Using Venus and Sentinel-2 Satellite Imagery. *Remote Sens.* **2020**, *12*, 352. [[CrossRef](#)]
12. Gao, F.; Anderson, M.; Daughtry, C.; Karnieli, A.; Hively, D.; Kustas, W. A Within-Season Approach for Detecting Early Growth Stages in Corn and Soybean Using High Temporal and Spatial Resolution Imagery. *Remote Sens. Environ.* **2020**, *242*, 111752. [[CrossRef](#)]
13. Thieme, A.; Yadav, S.; Oddo, P.C.; Fitz, J.M.; McCartney, S.; King, L.A.; Keppler, J.; McCarty, G.W.; Hively, W.D. Using NASA Earth Observations and Google Earth Engine to Map Winter Cover Crop Conservation Performance in the Chesapeake Bay Watershed. *Remote Sens. Environ.* **2020**, *248*, 111943. [[CrossRef](#)]
14. Prabhakara, K.; Hively, W.D.; McCarty, G.W. International Journal of Applied Earth Observation and Geoinformation Evaluating the Relationship between Biomass, Percent Groundcover and Remote Sensing Indices across Six Winter Cover Crop Fields in Maryland, United States. *Int. J. Appl. Earth Obs. Geoinf.* **2015**, *39*, 88–102. [[CrossRef](#)]
15. Hively, W.D.; Lee, S.; Sadeghi, A.M.; McCarty, G.W.; Lamb, B.T.; Soroka, A.; Keppler, J.; Yeo, I.Y.; Moglen, G.E. Estimating the Effect of Winter Cover Crops on Nitrogen Leaching Using Cost-Share Enrollment Data, Satellite Remote Sensing, and Soil and Water Assessment Tool (SWAT) Modeling. *J. Soil Water Conserv.* **2020**, *75*, 362–375. [[CrossRef](#)]
16. Yuan, M.; Burjel, J.C.; Isermann, J.; Goeser, N.J.; Pittelkow, C.M. Unmanned Aerial Vehicle-Based Assessment of Cover Crop Biomass and Nitrogen Uptake Variability. *J. Soil Water Conserv.* **2019**, *74*, 350–359. [[CrossRef](#)]
17. Roth, L.; Streit, B. Predicting Cover Crop Biomass by Lightweight UAS-Based RGB and NIR Photography: An Applied Photogrammetric Approach. *Precis. Agric.* **2018**, *19*, 93–114. [[CrossRef](#)]
18. Hunt, E.; Hively, W.; McCarty, G.; Daughtry, C.; Forrester, P.; Kratochvil, R.; Carr, J.; Allen, N.; Fox-Rabinovitz, J.; Miller, C. NIR-Green-Blue High-Resolution Digital Images for Assessment of Winter Cover Crop Biomass. *GIScience Remote Sens.* **2011**, *48*, 86–98. [[CrossRef](#)]
19. Goffart, D.; Curnel, Y.; Planchon, V.; Goffart, J.P.; Defourny, P. Field-Scale Assessment of Belgian Winter Cover Crops Biomass Based on Sentinel-2 Data. *Eur. J. Agron.* **2021**, *126*, 126278. [[CrossRef](#)]
20. Gausman, H.W. *Plant Leaf Optical Properties in Visible and Near-Infrared Light*; Texas Tech University Libraries: Lubbock, TX, USA, 1985.
21. Broge, N.H.; Leblanc, E. Comparing Prediction Power and Stability of Broadband and Hyperspectral Vegetation Indices for Estimation of Green Leaf Area Index and Canopy Chlorophyll Density. *Remote Sens. Environ.* **2001**, *76*, 156–172. [[CrossRef](#)]
22. Tucker, C.J. Red and Photographic Infrared Linear Combinations for Monitoring Vegetation. *Remote Sens. Environ.* **1979**, *8*, 127–150. [[CrossRef](#)]
23. Baret, F.; Guyot, G. Potentials and Limits of Vegetation Indices for LAI and APAR Assessment. *Remote Sens. Environ.* **1991**, *35*, 161–173. [[CrossRef](#)]
24. Mutanga, O.; Skidmore, A.K. Narrow Band Vegetation Indices Overcome the Saturation Problem in Biomass Estimation. *Int. J. Remote Sens.* **2004**, *25*, 3999–4014. [[CrossRef](#)]
25. Delegido, J.; Verrelst, J.; Alonso, L.; Moreno, J. Evaluation of Sentinel-2 Red-Edge Bands for Empirical Estimation of Green LAI and Chlorophyll Content. *Sensors* **2011**, *11*, 7063–7081. [[CrossRef](#)] [[PubMed](#)]

26. Nguy-Robertson, A.L.; Gitelson, A.A. Algorithms for Estimating Green Leaf Area Index in C3 and C4 Crops for MODIS, Landsat TM/ETM+, MERIS, Sentinel MSI/OLCI, and Venüs Sensors. *Remote Sens. Lett.* **2015**, *6*, 360–369. [[CrossRef](#)]
27. Gitelson, A.; Merzlyak, M.N. Spectral Reflectance Changes Associated with Autumn Senescence of *Aesculus Hippocastanum* L. and *Acer Platanoides* L. Leaves. Spectral Features and Relation to Chlorophyll Estimation. *J. Plant Physiol.* **1994**, *143*, 286–292. [[CrossRef](#)]
28. Dong, T.; Liu, J.; Shang, J.; Qian, B.; Ma, B.; Kovacs, J.M.; Walters, D.; Jiao, X.; Geng, X.; Shi, Y. Assessment of Red-Edge Vegetation Indices for Crop Leaf Area Index Estimation. *Remote Sens. Environ.* **2019**, *222*, 133–143. [[CrossRef](#)]
29. Kamenova, I.; Dimitrov, P. Evaluation of Sentinel-2 Vegetation Indices for Prediction of LAI, FAPAR and FCover of Winter Wheat in Bulgaria. *Eur. J. Remote Sens.* **2021**, *54*, 89–108. [[CrossRef](#)]
30. Gitelson, A.; Rundquist, D.C.; Leavitt, B. Papers in Natural Resources Remote Estimation of Leaf Area Index and Green Leaf Biomass in Maize Canopies. *Geophys. Res. Lett.* **2003**, *30*, 1248. [[CrossRef](#)]
31. Kross, A.; McNairn, H.; Lapen, D.; Sunohara, M.; Champagne, C. Assessment of RapidEye Vegetation Indices for Estimation of Leaf Area Index and Biomass in Corn and Soybean Crops. *Int. J. Appl. Earth Obs. Geoinf.* **2015**, *34*, 235–248. [[CrossRef](#)]
32. Badgley, G.; Anderegg, L.D.L.; Berry, J.A.; Field, C.B. Terrestrial Gross Primary Production: Using NIRV to Scale from Site to Globe. *Glob. Change Biol.* **2019**, *25*, 3731–3740. [[CrossRef](#)]
33. Camps-Valls, G.; Campos-Taberner, M.; Moreno-Martínez, Á.; Walther, S.; Duveiller, G.; Cescatti, A.; Mahecha, M.D.; Muñoz-Marí, J.; García-Haro, F.J.; Guanter, L.; et al. A Unified Vegetation Index for Quantifying the Terrestrial Biosphere. *Sci. Adv.* **2021**, *7*, 1–11. [[CrossRef](#)] [[PubMed](#)]
34. Liu, C.; Chen, Z.; Shao, Y.; Chen, J.; Tuya, H.; Pan, H. Research Advances of SAR Remote Sensing for Agriculture Applications: A Review. *J. Integr. Agric.* **2019**, *18*, 506–525. [[CrossRef](#)]
35. Lopez-Sanchez, J.M.; Ballester-Berman, J.D. Potentials of Polarimetric SAR Interferometry for Agriculture Monitoring. *Radio Sci.* **2009**, *44*, 1–20. [[CrossRef](#)]
36. McNairn, H.; Brisco, B. The Application of C-Band Polarimetric SAR for Agriculture: A Review. *Can. J. Remote Sens.* **2004**, *30*, 525–542. [[CrossRef](#)]
37. Lopez-Sanchez, J.M.; Ballester-Berman, J.D.; Vicente-Guijalba, F.; Cloude, S.R.; McNairn, H.; Shang, J.; Skriver, H.; Jagdhuber, T.; Hajnsek, I.; Pottier, E.; et al. Agriculture and Wetland Applications. In *Polarimetric Synthetic Aperture Radar*; Springer: Berlin, Germany, 2021; pp. 119–178.
38. Betbeder, J.; Fieuzal, R.; Baup, F. Assimilation of LAI and Dry Biomass Data from Optical and SAR Images into an Agro-Meteorological Model to Estimate Soybean Yield. *IEEE J. Sel. Top. Appl. Earth Obs. Remote Sens.* **2016**, *9*, 2540–2553. [[CrossRef](#)]
39. Hosseini, M.; McNairn, H. Using Multi-Polarization C- and L-Band Synthetic Aperture Radar to Estimate Biomass and Soil Moisture of Wheat Fields. *Int. J. Appl. Earth Obs. Geoinf.* **2017**, *58*, 50–64. [[CrossRef](#)]
40. Kim, Y.; Jackson, T.; Bindlish, R.; Member, S.; Lee, H.; Hong, S. Radar Vegetation Index for Estimating the Vegetation Water Content of Rice and Soybean. *IEEE Geosci. Remote Sens. Lett.* **2012**, *9*, 564–568.
41. Jin, X.; Yang, G.; Xu, X.; Yang, H.; Feng, H.; Li, Z.; Shen, J.; Zhao, C.; Lan, Y. Combined Multi-Temporal Optical and Radar Parameters for Estimating LAI and Biomass in Winter Wheat Using HJ and RADARSAR-2 Data. *Remote Sens.* **2015**, *7*, 13251–13272. [[CrossRef](#)]
42. Nasirzadehdizaji, R.; Sanli, F.B.; Abdikan, S.; Cakir, Z. Sensitivity Analysis of Multi-Temporal Sentinel-1 SAR Parameters to Crop Height and Canopy Coverage. *Appl. Sci.* **2019**, *9*, 655. [[CrossRef](#)]
43. Reisi-Gahrouei, O.; Homayouni, S.; McNairn, H.; Hosseini, M.; Safari, A. Crop Biomass Estimation Using Multi Regression Analysis and Neural Networks from Multitemporal L-Band Polarimetric Synthetic Aperture Radar Data. *Int. J. Remote Sens.* **2019**, *40*, 6822–6840. [[CrossRef](#)]
44. Scott, C.P.; Lohman, R.B.; Jordan, T.E. InSAR Constraints on Soil Moisture Evolution after the March 2015 Extreme Precipitation Event in Chile. *Sci. Rep.* **2017**, *7*, 4903. [[CrossRef](#)] [[PubMed](#)]
45. Lavalley, M.; Hensley, S. Demonstration of Repeat-Pass POLINSAR Using UAVSAR: The RMOG Model. In Proceedings of the 2012 IEEE International Geoscience and Remote Sensing Symposium, Munich, Germany, 22–27 July 2012; pp. 5876–5879.
46. Engdahl, M.E.; Borgeaud, M.; Rast, M. The Use of ERS-1/2 Tandem Interferometric Coherence in the Estimation of Agricultural Crop Heights. *IEEE Trans. Geosci. Remote Sens.* **2001**, *39*, 1799–1806. [[CrossRef](#)]
47. Srivastava, H.S.; Patel, P.; Navalgund, R.R. Application Potentials of Synthetic Aperture Radar Interferometry for Land-Cover Mapping and Crop-Height Estimation. *Curr. Sci.* **2006**, *91*, 783–788.
48. Nasirzadehdizaji, R.; Cakir, Z.; Balik, F.; Abdikan, S.; Pepe, A.; Cal, F. Sentinel-1 Interferometric Coherence and Backscattering Analysis for Crop Monitoring. *Comput. Electron. Agric.* **2021**, *185*, 106118. [[CrossRef](#)]
49. Hosseini, M.; McNairn, H.; Mitchell, S.; Dingle Robertson, L.; Davidson, A.; Homayouni, S. Synthetic Aperture Radar and Optical Satellite Data for Estimating the Biomass of Corn. *Int. J. Appl. Earth Obs. Geoinf.* **2019**, *83*, 101933. [[CrossRef](#)]
50. Saberioon, M.M.; Amin, M.S.M.; Anuar, A.R.; Gholizadeh, A.; Wayayok, A.; Khairunniza-Bejo, S. Assessment of Rice Leaf Chlorophyll Content Using Visible Bands at Different Growth Stages at Both the Leaf and Canopy Scale. *Int. J. Appl. Earth Obs. Geoinf.* **2014**, *32*, 35–45. [[CrossRef](#)]
51. Mao, W.; Wang, Y.; Wang, Y. Real-Time Detection of between-Row Weeds Using Machine Vision. In Proceedings of the 2003 ASAE Annual Meeting, Las Vegas, NV, USA, 27–30 July 2003; p. 1.

52. Thornton, P.E.; Shrestha, R.; Thornton, M.; Kao, S.-C.; Wei, Y.; Wilson, B.E. Gridded Daily Weather Data for North America with Comprehensive Uncertainty Quantification. *Sci. Data* **2021**, *8*, 1–17. [[CrossRef](#)] [[PubMed](#)]
53. Thornton, P.E.; Running, S.W.; White, M.A. Generating Surfaces of Daily Meteorological Variables over Large Regions of Complex Terrain. *J. Hydrol.* **1997**, *190*, 214–251. [[CrossRef](#)]
54. Mirsky, S.B.; Curran, W.S.; Mortensen, D.A.; Ryan, M.R.; Shumway, D.L. Control of Cereal Rye with a Roller/Crimper as Influenced by Cover Crop Phenology. *Agron. J.* **2009**, *101*, 1589–1596. [[CrossRef](#)]
55. Jennewein, J.; Lamb, B.T.; Hively, W.D.; Thieme, A.; Mirsky, S. Winter Cover Crop Biomass Sampling at the Beltsville Agricultural Research Center, 2019–2021, with Corresponding Sentinel-1 and Sentinel-2 Derived Indices and Metrics. *U.S. Geol. Surv. Data Release* **2022**. [[CrossRef](#)]
56. Hijmans, R.J.; van Etten, J.; Cheng, J.; Mattiuzzi, M.; Sumner, M.; Greenberg, J.A.; Lamigueiro, O.P.; Bevan, A.; Racine, E.B.; Shortridge, A.; et al. Package ‘Raster’. *R Package* **2015**, 734.
57. Pebesma, E.J. Simple Features for R: Standardized Support for Spatial Vector Data. *R J.* **2018**, *10*, 439. [[CrossRef](#)]
58. R Core Team R: A Language and Environment for Statistical Computing 2021. Available online: <https://www.r-project.org/> (accessed on 1 February 2022).
59. Hunt, R.E.; Doraiswamy, P.C.; McMurtrey, J.E.; Daughtry, C.S.T.; Perry, E.M.; Akhmedov, B. A Visible Band Index for Remote Sensing Leaf Chlorophyll Content at the Canopy Scale. *Int. J. Appl. Earth Obs. Geoinf.* **2013**, *21*, 103–112. [[CrossRef](#)]
60. Gitelson, A.; Merzlyak, M.N. Quantitative Estimation of Chlorophyll-a Using Reflectance Spectra: Experiments with Autumn Chestnut and Maple Leaves. *J. Photochem. Photobiol. B Biol.* **1994**, *22*, 247–252. [[CrossRef](#)]
61. Sims, D.A.; Gamon, J.A. Relationships Between Leaf Pigment Content and Spectral Reflectance Across a Wide Range of Species, Leaf Structures and Developmental Stages Relationships between Leaf Pigment Content and Spectral Reflectance across a Wide Range of Species, Leaf Structu. *Remote Sens. Environ.* **2002**, *81*, 337–354. [[CrossRef](#)]
62. Gitelson, A.A.; Merzlyak, M.N. Remote Estimation of Chlorophyll Content in Higher Plant Leaves. *Int. J. Remote Sens.* **1997**, *18*, 2691–2697. [[CrossRef](#)]
63. Chen, P.-F.; Nicolas, T.; Wang, J.-H.; Philippe, V.; Huang, W.-J.; Li, B.-G. New Index for Crop Canopy Fresh Biomass Estimation. *Spectrosc. Spectr. Anal.* **2010**, *30*, 512–517.
64. Xu, M.; Lacey, C.G.; Armstrong, S.D. The Feasibility of Satellite Remote Sensing and Spatial Interpolation to Estimate Cover Crop Biomass and Nitrogen Uptake in a Small Watershed. *J. Soil Water Conserv.* **2018**, *73*, 682–692. [[CrossRef](#)]
65. Haboudane, D.; Miller, J.R.; Pattey, E.; Zarco-tejada, P.J.; Strachan, I.B. Hyperspectral Vegetation Indices and Novel Algorithms for Predicting Green LAI of Crop Canopies: Modeling and Validation in the Context of Precision Agriculture. *Remote Sens. Environ.* **2004**, *90*, 337–352. [[CrossRef](#)]
66. Trudel, M.; Charbonneau, F.; Leconte, R. Using RADARSAT-2 Polarimetric and ENVISAT-ASAR Dual-Polarization Data for Estimating Soil Moisture over Agricultural Fields. *Can. J. Remote Sens.* **2012**, *38*, 514–527. [[CrossRef](#)]
67. Stenberg, P.; Rautiainen, M.; Manninen, T.; Voipio, P.; Smolander, H. Reduced Simple Ratio Better than NDVI for Estimating LAI in Finnish Pine and Spruce Stands. *Silva Fenn.* **2004**, *38*, 3–14. [[CrossRef](#)]
68. Huete, A.R.; Liu, H.; van Leeuwen, W.J. The Use of Vegetation Indices in Forested Regions: Issues of Linearity and Saturation. In Proceedings of the IGARSS’97, 1997 IEEE International Geoscience and Remote Sensing Symposium Proceedings, Remote Sensing—A Scientific Vision for Sustainable Development, Singapore, 3–8 August 1997; IEEE: Piscataway Township, NJ, USA, 1997; Volume 4, pp. 1966–1968. [[CrossRef](#)]
69. Gao, B. NDWI A Normalized Difference Water Index for Remote Sensing of Vegetation Liquid Water From Space. *Remote Sens. Environ.* **1996**, *58*, 257–266. [[CrossRef](#)]
70. Gorelick, N.; Hancher, M.; Dixon, M.; Ilyushchenko, S.; Thau, D.; Moore, R. Google Earth Engine: Planetary-Scale Geospatial Analysis for Everyone. *Remote Sens. Environ.* **2017**, *202*, 18–27. [[CrossRef](#)]
71. ASF DAAC. *Copernicus Sentinel Data*; ESA: Paris, France, 2021.
72. Cloude, S.R.; Pottier, E. Target Decomposition Ar Polarimetry. *IEEE Trans. Geosci. Remote Sens.* **1996**, *34*, 498–518. [[CrossRef](#)]
73. Cloude, S.R.; Pottier, E. An Entropy Based Classification Scheme for Land Applications of Polarimetric SAR. *IEEE Trans. Geosci. Remote Sens.* **1997**, *35*, 68–78. [[CrossRef](#)]
74. Cavanaugh, J.E. Unifying the Derivations for the Akaike and Corrected Akaike Information Criteria. *Stat. Probab. Lett.* **1997**, *33*, 201–208. [[CrossRef](#)]
75. Lenth, R.V. *emmeans: Estimated Marginal Means, Aka Least-Squares Means*. R Package Version 1.7.3. 2022. Available online: <https://CRAN.R-project.org/package=emmeans> (accessed on 1 February 2022).
76. Horler, D.N.H.; Dockray, M.; Barber, J. The Red Edge of Plant Leaf Reflectance. *Int. J. Remote Sens.* **1983**, *4*, 273–288. [[CrossRef](#)]
77. French, C.S.; Brown, J.S.; Lawrence, M.C. Four Universal Forms of Chlorophyll A. *Plant Physiol.* **1972**, *49*, 421–429. [[CrossRef](#)] [[PubMed](#)]
78. Thieme, A.; Hively, W.D.; Gao, F.; Jennewein, J.; Mirsky, S.; Soroka, A.; Keppler, J.; Bradley, D.; Thieme, A.; Hively, W.D.; et al. Remote sensing evaluation of Maryland winter cover crop delayed termination incentive. *Agronomy* **2022**. *manuscript in preparation*.
79. Gitelson, A.A.; Viña, A.; Ciganda, V.; Rundquist, D.C.; Arkebauer, T.J. Remote Estimation of Canopy Chlorophyll Content in Crops. *Geophys. Res. Lett.* **2005**, *32*, 1–4. [[CrossRef](#)]

80. Shang, J.; Liu, J.; Ma, B.; Zhao, T.; Jiao, X.; Geng, X.; Huffman, T.; Kovacs, J.M.; Walters, D. Mapping Spatial Variability of Crop Growth Conditions Using RapidEye Data in Northern Ontario, Canada. *Remote Sens. Environ.* **2015**, *168*, 113–125. [[CrossRef](#)]
81. Nilson, T. A Theoretical Analysis of the Frequency of Gaps in Plant Stands. *Agric. Meteorol.* **1971**, *8*, 25–38. [[CrossRef](#)]
82. Wegmüller, U.; Werner, C. Retrieval of Vegetation Parameters with SAR Interferometry. *IEEE Trans. Geosci. Remote Sens.* **1997**, *35*, 18–24. [[CrossRef](#)]
83. Ji, K.; Wu, Y. Scattering Mechanism Extraction by a Modified Cloude-Pottier Decomposition for Dual Polarization SAR. *Remote Sens.* **2015**, *7*, 7447–7470. [[CrossRef](#)]
84. Charbonneau, F.T.; Brisco, B.; Raney, R.K.; McNairn, H.; Liu, C.; Vachon, P.W.; Shang, J.; DeAbreu, R.; Champagne, C.; Merzouki, A.; et al. Compact Polarimetry Overview and Applications Assessment. *Can. J. Remote Sens.* **2010**, *36*, S298–S315. [[CrossRef](#)]
85. Mandal, D.; Kumar, V.; Ratha, D.; Dey, S. Dual Polarimetric Radar Vegetation Index for Crop Growth Monitoring Using Sentinel-1 SAR Data. *Remote Sens. Environ.* **2020**, *247*, 111954. [[CrossRef](#)]
86. Davitt, A.; Winter, J.M.; McDonald, K. Integrated Crop Growth and Radiometric Modeling to Support Sentinel Synthetic Aperture Radar Observations of Agricultural Fields. *J. Appl. Remote Sens.* **2020**, *14*, 1–25. [[CrossRef](#)]
87. Balenzano, A.; Mattia, F.; Satalino, G.; Davidson, M. Soil Moisture Retrieval from Dense Temporal Series of C-Band SAR Data over Agricultural Sites. *Int. Geosci. Remote Sens. Symp.* **2011**, *4*, 439–450. [[CrossRef](#)]
88. El Hajj, M.; Baghdadi, N.; Bazzi, H.; Zribi, M. Penetration Analysis of SAR Signals in the C and L Bands for Wheat, Maize, and Grasslands. *Remote Sens.* **2019**, *11*, 31. [[CrossRef](#)]
89. Satalino, G.; Mattia, F.; le Toan, T.; Rinaldi, M. Multitemporal C-Band Radar Measurements on Wheat Fields. *IEEE Trans. Geosci. Remote Sens.* **2003**, *41*, 1551–1560. [[CrossRef](#)]